Mutation in the rat interleukin 34 gene impacts macrophage development, homeostasis and inflammation in the brain and periphery

Stephen Huang*[,1], Omkar L. Patkar*[,1], Sarah Schulze*[,1], Dylan Carter-Cusack[1], Susan Millard[1], Ginell Ranpura[1], Emma K. Green[1], Emma Maxwell, Jeeva Kanesarajah, Gary Cowin[2], Damion Stimson[3], Nyoman D. Kurniawan[3], Sahar Keshvari[1], Rachel Allavena[4], Jeeva Kanesarajah[5], Allison R. Pettit[1], Katharine M. Irvine[1], David A. Hume[1]

1 Mater Research Institute-UQ, Translational Research Institute, Woolloongabba, Brisbane, Australia 4102

2 National Imaging Facility, Centre for Advanced Imaging, Australian Institute for Bioengineering and Nanotechnology, The University of Queensland, St Lucia, Brisbane, Australia, 4067

3 Centre for Advanced Imaging, Australian Institute for Bioengineering and Nanotechnology, The University of Queensland, St Lucia, Brisbane, Australia, 4067

4 School of Veterinary Science, The University of Queensland, Gatton, QLD 4343, Australia

5 QIMR Berghofer Medical Research Institute, Brisbane, Australia

Corresponding Authors: Katharine.irvine@uq.edu.au, David.hume@uq.edu.au

Keywords: IL34, CSF1, Macrophages, CSF1R, rat immunology, Microglia

Author contributions:

SH, OLP, SS – designed the research, performed research and analysed the data. Contributed equally to this work and are co-lead authors.

DCC, SM, GR, EKG, EM, RA, GC, NK, SK, DS, JK – performed research and analysed data.

ARP- supervised and advised the research.

DAH, KMI - designed and supervised the research, wrote the manuscript and funded the research

Conflict of interest statement

Authors declare no conflict of interest

Acknowledgements

The authors would like to thank and acknowledge the team at The University of Queensland PACE Biological resources facility (BRF) for their assistance with husbandry, maintenance, care, and monitoring of animals. We would also like to thank and acknowledge the BRF staff at the QBI animal behavioural facility and Centre for Advance imaging for the monitoring, care and maintenance of animals. The authors acknowledge the scientific and technical assistance from the microscopy, flow cytometry, and histology core facilities at Translational Research Institute and the National Imaging Facility, a National Collaborative Research Infrastructure Strategy (NCRIS) capability, at the Centre for Advanced Imaging, Australian Institute for Bioengineering and Nanotechnology, University of Queensland. We thank Glenda Gobe for advice on the renal pathology model. This work was supported by funding from Mater Foundation and NHMRC Investigator Grant #2007850 to DAH.

Abstract

Interleukin-34 (IL34) and colony stimulating factor 1 (CSF1) signal through a shared receptor (CSF1R) to control macrophage survival, differentiation and function. Here we describe the impact of loss of function mutation in the rat *Il34* gene. *Il34*$^{-/-}$ rats showed a partial reduction in macrophages within squamous epithelia (Langerhans-like cells) and in the testis. In the brain, microglia and brain-associated macrophages were selectively depleted in grey matter. A gradient of microglial density in *Il34*$^{-/-}$ cortex suggests that CSF1 can diffuse outwards from the corpus callosum. The reduced density of microglia was not associated with detectable neuropathology or behavioural alterations. In RNA-seq analysis of cortex, hippocampus and thalamus the only change is selective and uniform loss of the microglial signature. In the periphery, increased *Il34* expression has been associated with epithelial injury. In the adenine diet model of renal interstitial fibrosis both *Il34* and *Csf1* were induced. The absence of IL34 led to a significant reduction in macrophage recruitment compared to controls, but pathology assessed histologically or by detection of damage-associated mRNA signature was unaffected. We suggest that IL34 and CSF1 provide redundant signals to sustain microglia and to direct macrophage recruitment and repair tissue injury in the periphery.

53 Introduction

54 The mononuclear phagocyte system (MPS) is family of cells that includes committed hematopoietic
55 progenitors, blood monocytes and tissue resident macrophages that populate every organ in the body
56 (1-5). The proliferation, differentiation, function and survival of cells of the MPS is regulated by signals
57 from the macrophage colony-stimulating factor receptor (CSF1R). CSF1R expression is entirely
58 restricted to MPS cells and a knock-in transgenic reporter in mice highlights their abundance, location
59 and regular distribution in every organ (6). Homozygous loss of function mutations in the *CSF1R* locus
60 in mice, rats and humans are associated with depletion of MPS cells in most organs, including microglia
61 in the brain and bone-resorbing osteoclasts, and consequent severe pleiotropic impacts on postnatal
62 growth and development including osteopetrosis (7, 8). Resident tissue macrophages remain CSF1R-
63 dependent in adults and can be depleted by treatment with a blocking anti-CSF1R antibody (9).
64 CSF1R has two alternative ligands, CSF1 and IL34. Null mutations in the *Csf1* gene in mice and rats are
65 associated with tissue macrophage deficiency and osteopetrosis (10, 11). The existence of a second
66 CSF1R ligand was inferred from the age-dependent recovery of osteoclast function in CSF1-deficient
67 mice and the more severe phenotype observed in *Csf1r*$^{-/-}$ mice (12). Human IL34 was identified in 2008
68 (13). Subsequent studies revealed the functional conservation and co-evolution of the two CSF1R
69 ligands in birds (14, 15) and fish (16-19) and defined the molecular basis of binding of the two ligands
70 to the receptor (20). Although there have been several studies claiming differences in signalling
71 outcome in response to the two factors *in vitro* (21), they appear functionally equivalent *in vivo.*
72 Transgenic expression of IL34 from the *Csf1* promoter was sufficient to rescue all macrophage-
73 associated phenotypes in CSF1-deficient mice (22). In adult mice, *Il34* mRNA is expressed primarily in
74 the brain and epidermis and *Il34*$^{-/-}$ mice have a selective loss of microglia and Langerhans cells (23, 24).
75 IL34 has also been shown to regulate microglial colonisation of the brain in zebrafish (16, 18, 19). The
76 two ligands exhibit cell-specific and spatially-restricted expression in mouse brain (25); accordingly
77 administration of anti-IL34 antibody depleted microglia in grey matter whereas anti-CSF1 antibody
78 affected white matter microglia (26). Based upon conditional deletion of *Csf1* using nestin-cre, Kana

79 *et al.* (27) suggested that CSF1 was required specifically to maintain cerebellar microglia which were
80 required to regulate cerebellar development. Aside from CSF1R, IL34 has been shown to bind at least
81 3 additional putative receptors, PTPRZ1 (28), SYNDECAN1 (29) and TREM2 (30). However, at this time
82 no non-redundant biological activity of IL34 *in vivo* has been demonstrated to occur through receptors
83 other than CSF1R.
84 Increased expression of IL34 has been detected in a wide range of inflammatory diseases and
85 malignancies in patients (21, 31-43) but it remains unclear whether expression exacerbates or
86 mitigates pathology. One group has proposed that IL34 produced by regulatory T cells has a role in
87 transplant tolerance (44, 45). IL34 in mice has been implicated as an inducible mediator of tissue
88 damage in acute kidney injury (46) and in a lupus nephritis model (47). Conversely, rat models of renal
89 injury have emphasised inducible expression of CSF1 as a mediator (48, 49). Although these studies
90 have highlighted CSF1R as an anti-inflammatory drug target, CSF1 treatment actually promoted tissue
91 repair in kidney Ischaemia-reperfusion injury (50).
92 Rats have many advantages over mice as a model of human physiology and pathology (51). In terms
93 of CSF1R biology, there are clear differences in the impact of *Csf1* mutations between species. Unlike
94 $Csf1^{op/op}$ mice, $Csf1^{tl/tl}$ rats have an unremitting osteoclast deficiency and osteopetrosis but somatic
95 growth and male fertility is not affected (Reviewed in (51)). By contrast, homozygous mutation of the
96 rat *Csf1r* gene has a severe impact on postnatal growth and development (52, 53). These observations
97 suggested to us that the precise regulation and function of IL34 in control of MPS development,
98 homeostasis and immunopathology may differ between mammalian species. To investigate this
99 hypothesis, we created a null mutation in the *Il34* gene in the rat germ line. Analysis of the brain of
100 $Il34^{-/-}$ rats confirmed the selective loss of grey matter microglia observed with anti-IL34 treatment in
101 mice and provided evidence of haploinsufficiency. Gene expression profiling of multiple brain regions
102 indicated that there is little distinction between grey and white matter microglia, or selective gene
103 regulation by IL34. Based upon reported roles of IL34 in kidney inflammation in mice we compared
104 the response of wild-type and $Il34^{-/-}$ rats in a model of chronic renal injury. We conclude that IL34

105 exerts partly redundant control over recruited macrophages, but the absence of IL34 had no
106 detectable effect on either initial injury or repair. We conclude that IL34 is unlikely to be a target for
107 anti-inflammatory therapy.
108

109 ## Results

110 *Transcriptional regulation of Il34 in rats and humans*

111 Homozygous mutation of *Il34* in mice leads to selective depletion of microglia in the brain and
112 Langerhans cells in the epidermis (23, 24). Consistent with this pattern, amongst mouse tissues, *Il34*
113 is most highly-expressed in the brain and skin (see BioGPS.org). Genome-scale 5'RACE by the
114 FANTOM5 consortium revealed that expression in these two locations is driven by alternative tissue-
115 specific promoters (54). *Il34* mRNA is more widely-and uniformly expressed in human tissues (see
116 consensus data on www.proteinatlas.org) again involving separate transcription start sites (54). In
117 humans, a third TSS is utilised by a wide range of mesenchymal cell types. *Il34* mRNA is detected in
118 spleen in both humans and mice but not in lymphocytes in any state of activation (54). We recently
119 generated a transcriptional atlas for the rat by integrating 6700 RNA-seq datasets in the public domain
120 (55). We also generated a large RNA-seq dataset comparing gene expression in juvenile WT and
121 *Csf1rko* rats (56). As in humans, *Il34* mRNA is detected at comparable levels in most tissues in both
122 rat datasets; Figure S1A). To determine whether alternative promoter use was conserved, we mapped
123 RNA-seq reads from the entire rat atlas dataset to the rat genome as shown in Figure 1A**.** This analysis
124 indicated that as in mouse and human, neuronal tissues initiate transcription immediately 5' of the
125 first coding exon (CDS exon 1). In common with human, there is an alternative transcriptional start
126 site (TSS) associated with mesenchymal tissues. Skin tissue was poorly represented in the rat atlas but
127 transcripts were also detected coincident with the skin-specific 5' non-coding exon. This exon is
128 annotated on Ensembl and the sequence of the mouse skin-specific *Il34* promoter is conserved in rat
129 as well as human genomes.

130 *Phenotypic analysis of Il34$^{-/-}$ rats*

131 Since we commenced this project, Freuchet et al. (57) reported analysis of homozygous *Il34* frame-
132 shift mutation in exon 3 on an outbred Sprague-Dawley background. Their focus was on the proposed
133 function of IL34 in control of autoimmunity. They reported normal postnatal growth, reduced
134 microglia in the hippocampus, evidence of minor liver injury (marginal increase in circulating ALT, but

135 not AST or alkaline phosphatase), the presence of detectable auto-antibodies and increased
136 circulating CSF1. They also reported a selective reduction in $CD8^+$ T cells in the spleen.
137 The *Il34*$^{-/-}$rats on the inbred Fischer 344 background were generated by deletion of the 134bp second
138 coding exon using CRISPR-Cas9 (Figure S1F**)**. This deletion removes 35 amino acids of the active IL34
139 protein and introduces an in-frame stop codon at the start of the next exon. *Il34*$^{-/-}$ rats were born at
140 the expected Mendelian ratios. Although *Il34* mRNA is highly expressed by osteoblasts (55), as
141 reported previously (57) there was no significant impact of the *Il34* mutation on bone density
142 detectable by micro-computed tomography (μCT) (Figure 1B), by contrast to the severe unremitting
143 osteopetrosis observed in *Csf1*$^{tl/tl}$ rats (11). Unlike *Csf1r*$^{-/-}$ (52) and *Csf1*$^{-/-}$ (11) rats, postnatal somatic
144 growth was not affected in *Il34*$^{-/-}$ rats (Figure 1C), male-specific growth advantage post sexual maturity
145 was preserved and both males and females were fertile. *Csf1r*$^{-/-}$ rats have a partial loss of red pulp
146 macrophages in the spleen and complete absence of marginal zone ($CD169^+$) and marginal metallophil
147 ($CD209B^+$) populations, which are CSF1-dependent in mice (53). In the *Csf1r*$^{-/-}$ liver, Kupffer cells are
148 reduced by around 70% and the pericapsular macrophage population is absent (52). We found no
149 significant impact of IL34 deficiency on either liver population. In contrast to mouse, *Il34* mRNA is
150 highly-expressed in rat spleen (55). Splenic white matter topology and the location and abundance of
151 $IBA1^+$ and $CD209b^+$ macrophage populations was unaffected by the lack of IL34 **(**Figure 1D&E**)**. Given
152 the widespread expression of *Il34* mRNA we considered whether the absence might influence CSF1
153 homeostasis. Circulating CSF1 is regulated primarily by receptor-mediated endocytosis and
154 degradation by macrophages and is elevated in *Csf1r*$^{-/-}$ rats (52). However, serum CSF1 levels were
155 not altered in *Il34*$^{-/-}$ rats (Figure 1F).
156 Analysis of bone marrow, blood and spleen by Flow Cytometry revealed no significant differences in
157 the relative frequency of T cell, B cells, blood monocytes or granulocytes (Figure 1G, Figures S1B) in
158 *Il34*$^{-/-}$ rats compared to WT. In contrast to Freuchet et al, *Il34*$^{-/-}$ rats had a normal distribution of B cells,
159 CD4 and CD8 T cells in lymphoid organs, including spleen, thymus and cervical lymph node (Figure

160 S1C-E). These data indicate that the hematopoietic phenotype seen in the rat *Csf1r* mutation (52) is
161 also primarily due to loss of CSF1 rather than IL34 signalling.
162 To assess the effect of the IL34 knockout on tissue macrophage populations we crossed the mutation
163 to the *Csf1r*-mApple transgenic reporter line, which is expressed in all tissue macrophages and at lower
164 levels in granulocytes and B cells (58, 59). No gross differences in the distribution of tissue
165 macrophages were observed by wholemount imaging in any organ, including those in which *Il34*
166 mRNA is highly-expressed such as connective tissue, gut, muscle and thymus (55) (Figure 1H, Figure
167 S1F). By contrast to the reported loss of Langerhans cells in *Il34*$^{-/-}$ mice(23, 60), in *Il34*$^{-/-}$ rats there was
168 only partial reduction in the apparent density of Langerhans cells in stratified epithelia of the ear,
169 tongue, oesophagus and foot in adult and *Il34*$^{-/-}$ rats and the morphology was unaffected (Figure 2A).
170 Aside from the brain (see below), the only other location where we detected a clear loss of a
171 macrophage subpopulation was the testis, which contains three topologically-distinct populations,
172 interstitial and peritubular macrophages as described in the mouse (61-63) and a distinct
173 surface/subcapsular population. The surface and peritubular populations were relatively depleted in
174 *Il34*$^{-/-}$ rats (Figure 2B). Their loss is more readily appreciated through visualisation of 3 dimensional Z
175 stacks (Supplemental video files 1-2).
176 *The effect of Il34 mutation on microglial density, location and gene expression*
177 The brain contains two distinct populations of mononuclear phagocytes, classical microglia and brain-
178 associated macrophages (64) that line the vasculature and brain surfaces. Flow cytometry analysis of
179 leukocyte populations in disaggregated brain revealed that microglia (CD45^{low}/Cd11b/c^{high}) and brain-
180 associated macrophages (CD45^{high}/CD11b/c^{low}) were both significantly reduced in the *Il34*$^{-/-}$ brain
181 (Figure 2C). The relative abundance of both populations was reduced to a similar extent in
182 heterozygotes (*Il34*$^{+/-}$) indicating a lack of dosage compensation.
183 We next performed immunofluorescent staining on free floating sections to assess the morphology
184 and precise location of microglia in specific brain subregions. Figure 3A/Figure S2A show
185 representative images and Figure 3B/Figure S2B show quantitative analysis of IBA1^{+} cells in WT, *Il34*$^{+/-}$

186 and *Il34*$^{-/-}$ brains. There is clear depletion of classical highly-ramified microglia in defined grey matter
187 regions in IL34-deficient brain. The remaining microglia have a distinct morphology, apparently
188 aligned along the fibre tracts. This is particularly evident in the striatum. Interestingly, although the
189 global impact of IL34 deficiency in the cerebellum and brain stem is less obvious, ramified microglia
190 were clearly reduced. Consistent with the analysis in Figure 2, Figure 3 shows that microglial density
191 in multiple brain regions of *Il34*$^{+/-}$ rats was intermediate between wild-type and *Il34*$^{-/-}$ animals. The
192 microglia in this case remained evenly spaced but at a lower density. Figure 4A shows the density of
193 microglia in the multiple layers of the cortex from the corpus callosum to the meninges in the three
194 genotypes. In the *Il34*$^{-/-}$ brain, we noted an apparent outward gradient of microglial and perivascular
195 macrophage loss.
196 To confirm the conclusion from the Flow Cytometry profile that microglia and brain-associated
197 macrophages (BAM) were equally affected by the loss of IL34, we located the BAM marker CD163 (65)
198 on sections of cortex from wild type and *Il34*$^{-/-}$ brain. Figure 4B-F shows the selective loss of CD163^{+}
199 cells from the grey matter regions where microglia were also reduced but not from the meninges.
200 Taken together, the data demonstrate that IL34 and CSF1 are only partly compartmentalised within
201 the brain, each contributing to the local sustainable CSF1R-dependent mononuclear phagocyte
202 population.
203 To analyse the molecular consequences of microglial deficiency we profiled gene expression in the
204 cortex, hippocampus and thalamus of WT and *Il34*$^{-/-}$ rats at 10 weeks of age. The data are provided in
205 Table S1**.** Surprisingly, *Il34* mRNA is still detectable, reduced by around 50% in the mutant rats.
206 Mapping of the primary RNA-seq data to the rat genome confirmed the removal of the second coding
207 exon and generation of a spliced non-coding transcript that presumably does not undergo nonsense-
208 mediated decay.
209 Consistent with the loss of IBA1 staining in sections, *Aif1* mRNA was reduced by 40% in hippocampus
210 and thalamus and 60% in cortex. As in previous analysis of brain regions in *Csf1r*$^{-/-}$ rats (66) the
211 complete dataset was subjected to network analysis using *Graphia* to identify clusters of co-expressed

212 transcripts (Table S1). The only cluster clearly associated with IL34 genotype, Cluster 18, contains 80
213 transcripts including *Aif1* and *Csf1r* and overlaps with the microglial signature identified previously in
214 comparison of WT and *Csf1r*$^{-/-}$ rats (66). Figure 5A shows the average expression of genes within this
215 cluster, reduced by 40-60% in each brain region, which parallels the loss of *Aif1* and IBA1. We did not
216 detect expression of markers of damage-associated microglia (e.g *Clec7a*) or the loss of homeostatic
217 markers reported in *Il34*$^{-/-}$ mice (27, 67). Figure 5B shows the detection of individual transcripts,
218 confirming that homeostatic markers such as *P2ry12* and *Tmem119* were reduced to the same extent
219 as *Aif1, Csf1r, C1qa* and *Itgam.* Colocalisation of IBA1 and TMEM119 in cortex confirmed that the level
220 of expression in individual microglia is unchanged in the *Il34*$^{-/-}$ brain. (Figure 5C). Cluster 18 includes
221 three transcription factor genes, *Spi1, Irf5* and *Irf8,* but excludes *Sall1*, which is required for microglial
222 lineage identity (68, 69) (Figure 5D**).** Analysis of *Csf1r*$^{-/-}$ rat brains indicated that *Sall1* is not microglia-
223 restricted (66). Markers of brain-associated macrophages are more difficult to detect in total RNA-seq
224 data, but *Cd74* and *Cd68* were also reduced in *Il34*$^{-/-}$ brains. Separate sheets in Table S1 show
225 transcripts ranked based on IL34KO/WT ratio with known CSF1R-dependent microglia or macrophage-
226 associated transcripts highlighted.
227 In overview, the data demonstrate that the transcriptomic profiles of IL34-independent (i.e. CSF1-
228 dependent) microglial and BAM populations do not differ significantly from those of IL34-dependent
229 populations located mainly in grey matter.
230 *The effect of microglia deficiency on brain development and behaviour*
231 Dominant or recessive *CSF1R* mutations in humans are associated with microglial deficiency and
232 consequent neuropathology (70). By contrast to *Csf1r*$^{-/-}$ rat brains, the *Il34*$^{-/-}$ brains showed no
233 evidence of ventricular enlargement and the transcriptomic profiles did not include the induction of
234 stress response genes (e.g. *Rbm3, Mt1/2*) reported in the brains of juvenile *Csf1r*$^{-/-}$ rats (66) (Figure
235 S3A). In the hippocampus of *Csf1r*$^{-/-}$ rats we observed disorganised maturation of neuronal progenitors
236 stained with the marker doublecortin (DCX) but considered that this might be a consequence of stress
237 due to ventricular enlargement (66). Although microglia are depleted in the vicinity of the dentate

238 gyrus in *Il34*$^{-/-}$ brains, DCX staining did not distinguish wild type and mutant animals (Figure S3B, S3C).
239 Furthermore, in common with previous analysis of *Csf1r*$^{-/-}$ rat brains, the expression profiling did not
240 reveal any effect of the loss of grey matter microglia on astrocytes. The expression of *Gfap* mRNA and
241 the density, distribution and morphology of GFAP^{+} astrocytes was not affected by microglia deficiency
242 (Figure S3D&E).
243 One advantage of the rat is the wide range of human-relevant behaviour and functional tests
244 compared to mice (71). We subjected WT, *Il34*$^{+/-}$ and *Il34*$^{-/-}$ male and female rats to a battery of tests
245 between 4 and 6 months of age. We found no significant differences in performance in the sucrose
246 preference, O maze, open field and novel object recognition tests (Figure S4).
247 To look for age-dependent pathology resembling human leukodystrophy or neurodegeneration, we
248 analysed the same cohort at 18 months of age. Quantification of IBA1^{+} cells demonstrated that the
249 selective loss of microglia in cortex, hippocampus and thalamus in *Il34*$^{-/-}$ and partial depletion in *Il34*$^{+/-}$
250 rats was still present at 18 months (Figure S5A&B). Astrocytosis detectable by GFAP staining can be a
251 sensitive indicator of neuropathology, accelerated in microglia-deficient mice (72, 73). However, the
252 density and morphology of GFAP^{+} astrocytes remain unchanged in any brain region in the aged animals
253 (Figure S5C&D). In the cluster analysis, as a consequence of sample-to-sample variation in myelination,
254 oligodendrocyte-specific transcripts (e.g. *Olig1, Mbp*) form part of a single cluster, Cluster 6, that is
255 not correlated with *Il34* genotype. Diffusion tensor imaging revealed no significant effect of the lack
256 of IL34 on any white matter structure or the overall volume of any brain region (Figure S3F, Table S2).
257 Notably, there was no ventricular enlargement and no detectable flares in the thalamus suggestive of
258 calcification at this age. In addition, we assessed [^{18}F]DPA714 uptake by PET/MR to measure
259 neuroinflammation (74). This radioligand binds specifically to TSPO, a mitochondrial membrane
260 protein, and is used to detect neuroinflammation in human patients (74-79). We focussed our analysis
261 on the hippocampus, thalamus, pituitary and different cortex regions. We detected differences in
262 uptake between male and female animals consistent with previous reports (80) and a male specific

263 increase in uptake with age. However, there was no detectable difference in uptake between
264 genotypes (Table S3).
265 Recent studies have highlighted the relationship between microglial dyshomeostasis and the loss of
266 perineuronal nets (PNN) associated with cortical parvalbumin interneurons (81, 82). Proteoglycans
267 within these extracellular matrix structures can be detected by staining with *Wisteria floribunda*
268 *agglutinin* (WFA) and we localized parvalbumin (PV) neurons in the cortex. We found no significant
269 difference in WFA or PV staining between WT and IL34$^{-/-}$ rats (Figure S5E&F). Microglia-deficiency in
270 mice leads to reactive astrocytosis and extensive calcification in the thalamus detectable by 3-6
271 months of age and progressing in severity (83, 84). Consistent with the lack of detectable astrocytosis
272 in the thalamus of aged *Il34*$^{-/-}$ rats there was no calcification detectable by labelled risedronate staining
273 (**Data not shown**). In summary, the only significant difference detected between WT and *Il34*$^{-/-}$ brains
274 at any age examined is the selective loss of microglia in grey matter and associated reduction in
275 detectable microglia-specific transcripts.
276 **The role of IL34 in chronic inflammation in the kidney**
277 Network analysis of individual tissues with multiple region or state-specific RNA-seq data revealed a
278 strong correlation between *Il34* mRNA and a macrophage-specific signature in the kidney (55)
279 suggesting that IL34 does contribute to control of resident macrophage abundance in this organ. To
280 determine the role of IL34 in chronic renal inflammation, we established the rat adenine diet model
281 (85, 86), which leads to slowly progressive kidney damage with many features of chronic kidney
282 disease in humans including tubular atrophy, interstitial fibrosis and glomerulosclerosis. We exposed
283 cohorts of equal numbers of male and female WT and *Il34*$^{-/-}$ rats to an 0.2% adenine diet or normal
284 chow for 6 weeks. Both WT and *Il34*$^{-/-}$ rats had normal growth when placed on the adenine diet (Figure
285 6A). At a cage level, increased water consumption was evident by two weeks and by 5 weeks was more
286 than doubled for both male and female cages (Figure 6B&C). As reported previously (86) the effect of
287 the diet on renal function was gender-dependent. In males we detected increased serum creatinine

288 and blood urea nitrogen, whereas serum metabolites were not affected in females. These changes
289 were not significantly reduced in the *Il34*$^{-/-}$ males (Figure 6D&E).
290 A feature of the pathology in this model is the deposition of adenine crystals in the cortex, which
291 appeared reduced in females regardless of genotype, thickening of Bowman's capsule and mesangium
292 in glomeruli, loss of tubular brush borders; tubular atrophy and dilatation, expansion of interstitial
293 mononuclear cell populations and extensive fibrosis detected with Sirius Red (Figure 6F&G & Figure
294 S6). Glomerular pathology appeared male-specific perhaps associated with the observed gender
295 difference in clearance function. Quantitative analysis did not reveal any significant effects of the *Il34*
296 mutation, notably including the extensive interstitial fibrosis (Figure 6F&G).
297 We next asked whether the loss of IL34 had any effect on renal macrophage populations. Renal
298 macrophages can be detected by staining for IBA1 and IBA1^{+} cells are completely absent in the kidneys
299 of *Csf1r*$^{-/-}$ rats (52). There was a massive expansion of IBA1^{+} macrophage populations in the cortex and
300 medulla of rats on the adenine diet (Figure 7A&7B). Within the limits of quantification, the density of
301 renal IBA1^{+} cells in control animals was not significantly affected by the loss of IL34 but the response
302 to the adenine diet was reduced by around 50% (Figure 7D&7E). The presence of macrophages
303 expressing the haptoglobin receptor, CD163, has been associated with kidney injury in both animal
304 models and human disease and is commonly considered a marker of an anti-inflammatory phenotype
305 (87). In the adenine model, we detected expansion of a CD163^{+} cell population in the medulla only
306 which was significantly reduced in *Il34*$^{-/-}$ rats (Figure 7C&7F).
307 To further analyse the effect of the IL34 knockout on renal pathology, we performed total RNA-Seq
308 analysis of kidneys from wild-type and *Il34*$^{-/-}$ male control and adenine-fed rats. The complete dataset
309 is provided in Table S4**.** Separate Tabs show ranked lists of average expression comparing control
310 versus adenine-fed for each genotype and wild-type versus *Il34*$^{-/-}$ for the adenine-fed and control
311 animals. Table S4 also includes a highlights tab showing the data for selected adenine-regulated genes
312 in different functional groups that provide markers of pathology and an indication of the impact of the
313 *Il34* mutation. *Csf1* and *Il34* mRNA were each detectable in control kidney and increased >2 fold in

314 response to the adenine diet. Consistent with the reduced detection of IBA1^{+} cells *in situ*, the detection
315 of *Aif1* mRNA was increased ~6.5 fold in the kidneys of adenine-treated rats and this increase was
316 reduced significantly in the *Il34*$^{-/-}$ rats. Network analysis of the complete dataset is also shown in Table
317 S4**.** This analysis revealed a large cluster of 5879 transcripts (**Cluster 1**) with a shared pattern of up-
318 regulation in response to the adenine diet regardless of genotype, with a trend toward lower
319 expression in the *Il34*$^{-/-}$ rats. We recently identified the kidney resident macrophage signature by
320 comparing the transcriptional profiles of kidney from wild-type and *Csf1r*$^{-/-}$ rats (56). 158/166 CSF1R-
321 dependent transcripts identified by that analysis are contained within **Cluster 1** and are highlighted in
322 Red in Table S4**.** These transcripts were increased 4-40 fold in the kidney on the adenine diet and
323 reduced in *Il34*$^{-/-}$ rats compared to wild-type (ratio 0.27-0.68; mean 0.46). The individual data for
324 selected macrophage genes *Aif1, Adgre1, Csf1r, Clec10a, Mrc1 a*nd *C1qa* are shown in Figure S7A*.* One
325 other feature evident in Cluster 1 is the transcriptional signature of the cell division cycle. The cluster
326 contains 267/496 genes with known functions in the cell cycle (88) including *Mki67*. The overall
327 pattern indicates that the response to adenine involves expansion of macrophage populations with a
328 resident transcriptomic profile and that this expansion depends in part on induction of IL34. *Csf1* and
329 *Il34* are not the only inducible transcripts encoding myeloid growth factors in the injured kidney. *Ftl3lg*
330 mRNA was detected at a similar level and increased in response to adenine, likely driving expansion
331 of FLT3-expresssing classical dendritic cells (cDC1) and increased detection of markers *Flt3, Ccr7, Xcr1,*
332 *Itgae* and *Clec9a* (89) (Figure S7B). Although macrophages appear to be the dominant inflammatory
333 cell population, **Cluster 1** also includes numerous chemokines and signature genes indicating
334 recruitment of monocytes (*Cd14, Cyba*), T cells (*Cd3e/d/g*), and granulocytes (*S100a8/9*), each also
335 reduced in the *Il34*$^{-/-}$*.*
336 The tubular pathology and interstitial fibrosis observed in tissue sections is associated with markedly
337 increased detection of markers of epithelial injury including cytokeratins (*Krt7/8/18/19* (90)), *Havcr1*
338 (aka Kidney Injury Marker 1), *Spp1* (osteopontin) and *Mmp7* (91) and of myofibroblasts (e.g. *Acta2,*
339 *Col4a1, Mgp*). Cytokines *Il19* and *Il24,* implicated in epithelial injury and fibrosis in human kidney

340 disease and in mouse models (92, 93) were almost undetectable in control and strongly-expressed in
341 diseased kidney. Consistent with evidence of inflammasome activation in crystal-induced
342 nephropathy (94), *Il1b* and *Il18* were each increased. Epithelial loss or dysfunction is indicated by
343 reduced detection of tubule markers such as *Umod, Slc12a1* and *Slc21a4* defined in the rat
344 transcriptomic atlas (55). Within the constraints of inter-individual variation, there was no significant
345 difference in detection of any of these markers of pathology between the wild-type and *Il34*$^{-/-}$ rats on
346 the adenine diet (Table S4).
347 The histopathology and RNA-seq analysis indicate that IL34-dependent expansion of resident
348 macrophages is not a driver of tubular damage or fibrosis. The alternative possibility is that it is a
349 response to injury and associated with repair. To address this possibility, we looked at recovery from
350 the adenine diet. Wild type and *Il34*$^{-/-}$ rats were fed the diet for 6 weeks then transferred to normal
351 chow for 4 weeks. Following transfer to normal chow, both groups continued to grow normally. Serum
352 creatinine and BUN trended downwards towards control levels but remained elevated independent
353 of genotype (Figure S8A&B). The expression of *Cd163* mRNA in wild-type animals returned to baseline
354 and fibrosis scores based upon Sirius red staining also showed evidence of recovery but there was no
355 difference between wild-type and *Il34*$^{-/-}$ rats (Figure S8C&D). In summary, the adenine-induced renal
356 pathology was slowly reversed following removal of the diet but reversal was not altered by the
357 absence of IL34.
358

359 Discussion

360 A previous analysis of the phenotype of an *Il34* mutation in rats (57) was focussed on the putative
361 expression of IL34 by regulatory T cells (Treg) and a role in autoimmunity (44, 45). The expression of
362 *IL34* mRNA reported in rat and human T cells was detected by qRT-PCR and in humans by Flow
363 Cytometry. The conclusion that IL34 is a T cell lymphokine is not supported by other evidence. *IL34*
364 mRNA is not detectable in human Treg in bulk (54, 95) or single cell RNA-seq data (96) and was not
365 detected in either CD4 or CD8 rat Treg isolated using a *Foxp3*-EGFP reporter by the same group (97).
366 We were not able to reproduce the apparent loss of CD8 T cells reported in *Il34*$^{-/-}$ rats (57). Indeed, we
367 found no detectable effect on leukocyte populations in the steady state. Similarly, no change in
368 relative abundance of T cell populations was detected in *Il34*$^{-/-}$ mice (24).

369 In mice, *Il34* mRNA is expressed selectively in epidermis and brain, whereas *Csf1* is expressed in
370 mesenchymal cells and undetectable in epidermis (biogps.org). By contrast, in rats *Il34* mRNA is widely
371 expressed. In the rat skin *Il34* and *Csf1* mRNA are expressed at similar levels (biogps.org/ratatlas)
372 although the separation of dermis and epidermis has not been reported. In the mouse, Langerhans
373 cells in the epidermis of the ear were almost entirely IL34-dependent (23, 24). Other squamous
374 epithelia were not examined. In the *Il34*$^{-/-}$ rat, intraepithelial Langerhans-like cells in squamous
375 epithelia were only partly depleted compared to WT (Figure 2A).

376 The main location where the loss of IL34 impacted resident tissue MPS populations is the brain. A
377 detailed analysis of microglial location and morphology in mice (98) indicated the relatively low
378 density of F4/80^{+} cells in white matter and fibre tracts, and the unique morphology aligned along the
379 fibres. In common with humans (99), microglia in rat brain are equally abundant in white and grey
380 matter, but in white matter they have the same elongated morphology described in mice. Consistent
381 with the reported effect of anti-IL34 and anti-CSF1 treatment in adult mice (26), we observed selective
382 loss of microglia in grey matter in *Il34*$^{-/-}$ rats but the effect was subtle. Within the grey matter regions,
383 CD163^{+} perivascular macrophages were also depleted but the remaining IBA1^{+} cells occupied a distinct
384 location. Because of their relative abundance, the retention of morphologically distinct microglia,

385 elongated along the fibre tracts, is obvious in the rat especially in the striatum. In comparison to rats,
386 the *Il34* mutation in mice had a greater overall impact on microglial density, including a reduced
387 density in the corpus callosum, and the residual microglia were not morphologically distinct (23, 24).
388 Kana *et al.* (27) reported the impact of conditional *Csf1* deletion in mouse brain which produced
389 selective microglial depletion in the cerebellum. Although *Csf1* is more highly-expressed in the rat
390 cerebellum than *Il34,* there was also selective loss of microglia within grey matter in this region and in
391 the brain stem in the *Il34*$^{-/-}$ rats (Figure 3). This was not detected in *Il34*$^{-/-}$ mice (23, 24). Finally, we
392 report for the first time that IL34 deficiency is not dosage compensated and *Il34*$^{+/-}$ rats have a partial
393 loss of grey matter microglia. In common with the reduced density of microglia in mice with a
394 heterozygous dominant-negative *Csf1r* mutation (100) the residual microglia in the *Il34*$^{-/-}$ rat brain are
395 evenly spaced. The regular distribution of macrophages in tissues has been attributed to competition
396 for growth factors and mutual repulsion, so that macrophages (including microglia) are autonomous
397 and occupy a territory rather than a precise niche (2). The strict compartmentalisation of IL34 and
398 CSF1 implied from analysis of *Il34*$^{-/-}$ mice (23, 24) is clearly not the case in the rat. The gradient of
399 microglial loss observed in the cortex (Figure 4A) suggests that CSF1 produced in corpus callosum is
400 able to diffuse outward to partly compensate for the loss of IL34 (101).
401 The expression profiling of the brain of *Il34*$^{-/-}$ rats revealed the coordinated partial loss of microglia-
402 associated signature transcripts previously identified as CSF1R-dependent from analysis of multiple
403 brain regions in *Csf1r*$^{-/-}$ rats (66). The thalamus was included because of recent evidence that the loss
404 of microglia in mice leads to calcification of this brain region (83, 84). Aside from the loss of the
405 microglial signature, we did not detect significant changes in expression of any transcripts that would
406 indicate either a neurodevelopmental defect or pathology. This observation provides evidence against
407 a CSF1R-independent function of IL34 mediated through binding to PTPRZ1, which is expressed
408 specifically by neurons (28). The absence of microglia in mice with a hypomorphic *Csf1r* mutation also
409 leads to progressive demyelination, which has been analysed as a model for leukodystrophy
410 associated with human *CSF1R* mutation (83, 102). Not surprisingly, since white matter microglia are

411 largely spared, we did not detect changes in myelin in the *Il34*$^{-/-}$ rat. Whilst it is difficult to prove the
412 absence of an effect, *Il34*$^{-/-}$ rats were not distinguishable from wild-type littermates in brain imaging
413 and in a wide range of behavioural tests. Similarly, the density of perineuronal nets, a morphological
414 surrogate for neuronal plasticity in the cortex that is regulated by microglia in mice (81, 103) was not
415 altered in *Il34*$^{-/-}$ rats. In overview, the analysis supports the view that microglial functions in
416 neurodevelopment are redundant (66, 104). Their clear essential function in mice is in the mitigation
417 of neuropathology (23, 24, 72, 73, 83, 102, 105). Interestingly, a relatively common stop-gain mutation
418 in human *IL34* (Y213Ter, minor allele frequency ca. 0.1) has been associated with an increased relative
419 risk of developing Alzheimer's disease (106). This variant lies downstream of the active IL34 peptide,
420 so the functional impact on active IL34 generation is not known. IL34 amino acid sequence is highly
421 conserved in mammals and birds (15) but available human exome sequences
422 (https://gnomad.broadinstitute.org/) highlight multiple coding variants within the active peptide in
423 human populations. The lack of dosage compensation and partial loss of microglia in *Il34*$^{+/-}$ rats
424 indicates that heterozygous loss of function *IL34* mutation could impact microglia in humans. Equally,
425 since homozygous mutants are viable, long-lived and fertile, homozygous loss of function in humans
426 may be tolerated. The *Il34*$^{-/-}$ rat provides a model in which to dissect the specific functions of microglia
427 that more closely approximates human biology.
428 The emerging literature on IL34 views it as a pro-inflammatory cytokine and therefore a potential
429 target in inflammatory disease (21, 42). Whilst there is clear evidence of an association between
430 increased detection of IL34 and disease severity in a range of human inflammatory diseases, evidence
431 of function is more equivocal and almost entirely based on mouse models. For example, Baek *et al.*
432 (46) reported that IL34 generated by tubular epithelial cells (TECs) promoted macrophage-mediated
433 acute epithelial injury in a kidney ischemia reperfusion model and exacerbated subsequent chronic
434 fibrotic disease. This report is difficult to reconcile with the trophic effects of the alternative CSF1R
435 ligand, CSF1, in the same model (50). Our comparative analysis of chronic renal injury in the wild-type
436 and *Il34*$^{-/-}$ rats does not support the view that IL34 is an essential mediator of tissue injury. In wild-

437 type rats in the adenine model we detected induction of both *Il34* and *Csf1* mRNA, increased
438 abundance of interstitial macrophages, and increased detection of numerous transcripts expressed
439 specifically by resident kidney macrophage populations. Previous studies have demonstrated that
440 inducible expression of CSF1 drives local macrophage proliferation in response to renal injury in rats
441 (48, 49). The relative density of IBA1^{+} cells, and detection of resident macrophage-associated
442 transcripts, was approximately halved in the *Il34*$^{-/-}$ rats. The simplest explanation is that the two
443 inducible CSF1R agonists are partly redundant. FLT3-ligand may also contribute to expansion of
444 interstitial mononuclear phagocyte populations. We observed increased expression of *Flt3lg* mRNA
445 and of transcripts associated with classical dendritic cells in response to the adenine diet (Table S4)
446 There has been significant debate in the literature as to whether to classify renal interstitial myeloid
447 populations as macrophages or DC based on surface markers (89, 107). Interestingly, expression
448 profiling of kidneys of *Csf1r*$^{-/-}$ rats revealed 80% loss of *Flt3* mRNA suggesting that renal interstitial
449 myeloid cells may be unique in expressing both FLT3 and CSF1R (56).
450 Whereas the absence of IL34 compromised interstitial macrophage expansion in the injured kidney
451 (Figure 7), it had no significant impact on any aspect of pathology, including clearance functions, overt
452 pathology or the expression of damage-associated transcripts (Table S4). Furthermore, the slow
453 recovery following removal of the adenine diet was neither prevented nor accelerated. CSF1 and IL34
454 are also both induced following epithelial injury in the intestine, including in human ulcerative colitis
455 (43). In both rats and mice, IL34 deficiency caused a moderate increase in pathology in the dextran
456 sodium sulphate colitis model (43, 57, 108). Taking all of the evidence together, we suggest that
457 increased expression of CSF1R ligands is a consequence rather than a cause of pathology associated
458 with chronic tissue injury that serves to promote resolution. That conclusion would imply that
459 treatment with antagonists of either ligand or the receptor is unlikely to be therapeutic in
460 inflammatory disease and may actually exacerbate or prolong the injury.
461

462 ## Methods and Materials

463 *Sex as a biological variable*

464 Both male and female animals were used unless otherwise stated.

465 *Animals*

466 IL34 knockout rats were generated under contract by Taconic Biosciences (Germantown, NY, US)
467 through CRISPR mediated recombination with guide RNAs flanking exon 2 of the *Il34* gene (Figure
468 S1G). Animals carrying the knockout allele were imported to Australia, rederived into a specified
469 pathogen-free (SPF) facility and maintained on the F344/DuCRL background. Deletion of exon 2 was
470 confirmed by PCR using flanking primers (5'TTTAGCATCTCAGAGCCATCAG (forward),
471 5'GCAGCTTGACAACAGACAGG (reverse) giving products of 1541bp (WT) and 353bp (Mut). The same
472 primers were used for genotyping.

473 There are no gross morphological differences in the IL34 homozygous or heterozygous animals and
474 both male and female animals are fertile. Rats between 8-10 weeks of age were used to characterize
475 distribution and morphology of macrophages unless stated otherwise. Rats for behavioural tests were
476 4 months of age at the time of behavioural testing and 6 months of age for PET/MR scanning. A cohort
477 of animals were aged a minimum of 18 months (18-26 months) and also underwent PET/MR scanning.
478 For whole mount imaging, *Il34*$^{-/-}$ rats were crossed with the *Csf1r*-mApple transgenic reporter line (58).
479 F1 progeny were interbred and F2 animals 8-10 weeks of age were used for analysis.

480 All animals were housed in ventilated cages at 21°C at a relative humidity of 76% and provided
481 standard chow and water *Ad libitum*. All animal procedures were performed at The University of
482 Queensland under protocols approved by the Institutional Animal Ethics Unit (UQ AE2022/000676,
483 AE2021/000337, AE2022/00066, and AE2022/000191).

484 *Adenine induced chronic kidney injury model*

485 Rats were 6 weeks of age at the beginning of the adenine diet. Adenine treated rats received R&M
486 0.2% Adenine Normal Feed (SF14-139, Specialty Feeds, Glen Forrest, WA) and water *Ad libitum* for 6

weeks while control animals were kept on standard chow. The recovery cohort also received adenine for 6 weeks and then were given standard chow for4 weeks.

Animal behaviour studies

Sucrose preference test

Animals were housed individually for 1 week prior to testing. A two bottle paradigm was set up for each cage with one bottle containing standard water and the second containing a 5% sucrose solution diluted in the standard drinking water. Bottles were weighed prior to testing and after removal. Animals began testing at 6pm each evening and bottles were replaced with standard water the following morning at 6am and animals were tested again between 6pm-6am with bottle positions swapped.

Open field test

Animals were placed in the centre of a 56cm square arena and allowed to explore for 10 minutes. A border 10cm from the edge was considered the border boundary and the remaining space within the square was considered the central area. Time spent within the central area was quantified when the centre of the animal's body occupied this space.

Novel object recognition

Novel object recognition assays were performed in a 112x56cm arena. Two pyramidal objects were placed 26cm from the edges of the arena for the learning phase which occurred over 2 days. Animals were placed in the centre of the arena and allowed to explore for 10 minutes. On the third day one object was replaced with an ellipsoid-shaped object and animals were placed in the centre and allowed to explore for 10 minutes. Time interacting with objects was quantified when the nose of the animal was within the boundaries of each object.

Elevated O-maze

The platform is a circular disc approximately 120cm in diameter. The platform width was approximately 10cm and elevated 60cm above the ground. The closed arms of the O-maze consisted

512 of walls that were 30cm tall. Animals were placed in the centre of the open arms and allowed to
513 explore for 10 minutes. Total animal movement and time spent in the open arms were quantified.

514 *MicroCT analysis of bone*

515 Whole right hind limbs were fixed in 4%PFA/PBS for 6 days at 4°C and then transferred into PBS and
516 scanned using Bruker SkyScan 1272. All x-ray projections were reconstructed in a blinded manner
517 using a modified back-projection reconstruction algorithm (NRecon 1.7.3.1 software (SkyScan; Bruker
518 µCT) to create cross-sectional images, and 3-dimensional (3D) reconstructions were viewed using
519 CTvox 3.3.0 (Bruker µCT). Reconstructed images were then analyzed using CTAn 1.19 software
520 (Bruker), which has inherent 2D and 3D analysis tools (109).

521 *Flow cytometry and haematology*

522 Blood was collected via cardiac puncture into EDTA coated minicollect tubes (Greiner, #450532) for
523 haematology or serum separator vacuette tubes (Greiner, #456010) for sera analysis. 100uL of blood
524 was treated with 1ml of red blood cell lysis buffer (0.15M NH4Cl, 10mM NaHCO3) for 2 minutes at
525 room temperature then washed in 10mL of PBS. Lysed preparations were then spun at 500g 5min 4C,
526 washed in 10mL of PBS and then resuspended in FACS buffer. Thymus, cervical lymph nodes (cLN),
527 spleen and bone marrow were collected in FACS buffer (2%FCS/PBS) and filtered through a 40 µM
528 filter to produce single cell suspension. Splenic cell preparations were treated with red blood cell lysis
529 buffer. All single cell preparations were enumerated and $1x10^6$ cells were stained for 30min at 4°C.
530 Brain tissue for flow cytometry was collected from one hemisphere by performing a sagittal incision
531 down the midline of the brain. This tissue was then minced with a scalpel in a petri dish, resuspended
532 in HBSS containing collagenase type IV (1mg/mL), dispase (0.1mg/mL), and DNase1 (19mg/mL), and
533 incubated on a rocking platform for 45 min at 37°C. The tissue was then passed through a 70µm filter,
534 washed in 25mL PBS and centrifuged (at 400g and 4°C for 5 min). Supernatant was removed and the
535 pellet resuspended in 12.5mL isotonic Percoll (2.44mL Percoll (Cytiva, MA, USA), 0.47mL 10x PBS,
536 7.815mL 1x PBS). The suspension was centrifuged at 800g for 45 min (no brake) at 4°C. The

537 supernatant containing the top myelin layer was aspirated, and the pellet was washed twice with PBS,
538 and finally resuspended in flow cytometry (FC) buffer (PBS/2% FCS).
539 The following antibody panel was used across tissue preparations:

	Panel 1	Panel 2
Antibodies	CD32 HIS48-FITC CD11B/C-BV510 CD45R-BV785 CD172-BV421 CD45-PE/Cy7 CD43-AF647 CD4-APC/Cy7 7AAD	CD32 CD3- FITC CD4-APC/Cy7 CD8-APC CD45R-BV785 7AAD
Tissues profiled	Brain, Bone marrow, Spleen and Blood	Cervical lymph nodes and Thymus

540 Flow cytometry data was acquired on an Fortessa X20 Cytometer (BD Biosciences, NJ, USA), and data
541 was analysed using FlowJo v10 Software (BD Life Sciences, NJ, USA). Live single cells were gated and
542 subsequent populations defined by the gating strategy illustrated in Figure S9.
543 *Histochemical staining and immunolocalisation*
544 Spleens, livers and kidneys were collected and washed in PBS before fixing in 4%PFA for 24 hours at
545 room temperature then processed and embedded into paraffin using routine methods. 4μM and
546 10μM sections were deparaffinised and rehydrated with standard methods; xylene followed by
547 descending ethanol series. 4μM sections were used for Sirius red and Hematoxylin and Eosin (H&E)
548 staining and 10μM sections for immunohistochemical staining as previously described (56, 110).
549 Briefly, sections were stained with Gill's No. 2 haematoxylin for 30 seconds and eosin for 40 seconds
550 for H&E staining and for Sirius red staining, sections were stained in Picric-Sirius Red solution

551 (Australian Biostain P/L, VIC, Australia) for 1hr. Heat-induced epitope retrieval was performed in 10
552 mM Sodium Citrate Buffer (pH6.0) followed by staining with rabbit anti-IBA1 (FUJIFILM, WAKO
553 chemicals, Richmond, Virginia, USA, 019-19741, 1:1000). 10mM EDTA buffer (pH 9.0) was used for
554 antigen retrieval for rabbit anti-CD163 (Abcam, ab182422, ERP19518, 1:500) and CD209B (Abcam,
555 ab308457,1:2000). Detection was performed with DAKO Envision Anti-rabbit HRP detection reagent
556 (Agilent). Sections were dehydrated in increasing ethanol series, cleared in xylene and coverslips
557 mounted with DPX mountant (Sigma). Whole slide digital scanning was performed on the VS120 or
558 VS200 at 40x objective magnification.
559 Free-floating sections of brain were generated and immunolocalisation of markers was performed as
560 described previously (66). For the older animals (>18 months), tissues were fixed by transcardial
561 perfusion with 4% paraformaldehyde in PBS and post fixed for 24hours at room temperature in
562 4%PFA/PBS. For analysis of young adult brains, sections were stained and imaged on Olympus FV3000
563 microscope as confocal images on either on the 40x or 60x oil objective with z stacks using solid state
564 lasers (405, 488 and 647 nm) for each brain region as follows:

Protein marker	**Antibody details**	**Cell identification**	**Objective used**	**Stacks**
IBA1	Wako Cat # 01-1874	Microglia	40× air	12
GFAP	Invitrogen Cat # PA1-10004	Astroglia	40× air	20
DCX	Cell signalling 4604s	Immature neurons	40× air and 60× oil	20 and 30
CD163	Abcam ab182422	Perivascular macrophages	40× air	15
TMEM119	Synaptic system 400-004	Microglia	20× air	20

565

566 For analysis of aged animals (>18 months) sections were stained and imaged on Olympus FV3000
567 microscope as confocal images on either on the 4x, 10x or 20x oil objective with z stacks using solid
568 state lasers (405, 488 and 647 nm) for each brain region as follows:

Protein marker	Antibody details	Cell identification	Objective used	Stacks
IBA1	Novachem Cat # 019-19741	Microglia	10x air	30
GFAP	Invitrogen Cat # PA1-10004	Astroglia	4x air	40
WFA	VectorLabs Cat # ZH0824	Perineuronal nets	20x air	30
PV	Synaptic Systems Cat # 195004	Parvalbumin neurons	20x air	30
Risedronate	BioVinc LLC Cat # BV500101	Fluorescent bisphosphonate analogue	4x air	40

569

570 *Image analysis*

571 Images were taken as a z-stack of 1 µm thickness and converted to Z-project on Image J with FIJI
572 software (version 1.54f). A minimum of 4 images per brain section were analysed for either number
573 of positive cells (IBA1, PV) or percentage area (GFAP, WFA) as follows: Images were Z-projected and
574 converted to RGB image and colour thresholding was performed using either default method (Iba1,
575 GFAP) or MaxEntropy method (WFA, PV) with the same settings across genotypes. Raw data was
576 collected using the measure tool and values were plotted on GraphPad Prism (version 10.3.1).

577 *Diffusion Tensor imaging and analysis*

578 Fixed brains were washed in 0.1 M PBS for >1 week for scanning using a 16.4 T vertical bore MR
579 microimaging system (Bruker Biospin, rheinstetten, Germany; Paravision v6.01), equipped with a
580 Micro2.5 imaging gradient using a 20 mm linear surface acoustic wave coil (M2M, Brisbane, Australia).
581 3D T1/T2*-weighted multi gradient echo (MGE) images were acquired with TR = 70 ms, bandwidth =
582 100 KHz, FOV = 27 × 18 × 15 mm and matrix size = 216 × 144 × 120, resulting in 120 µm 3D isotropic
583 image resolution, with the acquisition time of 40 mins. The MGE data contained fifteen TEs (= 4, 8,12,
584 ... 60 ms) for Quantitative Susceptibility Mapping. Subsequently, samples were washed in 0.1 M PBS
585 with 0.2% v/v Magnevist (Bayer) for >1 week. 3D DWI data were acquired using a Stejskal-Tanner DWI
586 spin-echo sequence with TR = 200 ms, TE = 21 ms, δ/Δ = 2.5/12 ms, bandwidth = 50 KHz, FOV = 27 ×
587 18 × 15 mm and matrix size = 180 × 120 × 100, image resolution = 150 µm, 30 direction diffusion
588 encoding with b-value = 5000 s/mm2, three b = 0 images, with the acquisition time of 15 h 42 min.
589 Quantitative susceptibility maps (QSM) and T2* relaxation maps of the rat brains were calculated
590 using the program (QSMxT) (111). The anatomical images were constructed by combining multi-echo
591 images to enhance image contrast. Images were registered into the Waxholm Space MRI/DTI template
592 for the Sprague Dawley rat brain**,** using ANTs diffeomorphic image registration (112-114). The model-
593 based segmentation of brain regions was performed on each sample and their image volumes and
594 intensities were measured using ITK-SNAP.
595 The FID of DWI datasets were zero-filled by a factor of 1.5 in all dimensions prior to Fourier transform
596 to improve fibre tracking. DWI data were bias corrected using ANTs N4BiasFieldCorrection and
597 processed using MRtrix3 software (www.mrtrix.org). Fiber orientation distribution (FOD) was
598 reconstructed using constrained spherical deconvolution (CSD) method, and probabilistic
599 tractography was performed using iFOD2 algorithm. Tractography was performed for specific major
600 white matter (WM) tracts. Firstly, the seeding regions of interest (ROIs) were manually drawn in the
601 midsagittal and coronal sections of the colour vector map, and fibretracks were generated for the
602 corpus callosum (CC), hippocampal commissure (HC), internal capsule (IC) and anterior commissure

603 (AC) at 100 seeds per voxel. The volumes of the white matter tracts were measured from Tract Density
604 Intensity maps (TDI) with the intensity threshold set at 20% to remove background noise from
605 probabilistic tracking (112, 115).

606 *PET/MR imaging of DPA714 uptake*

607 DPA714-F18 was synthesized as previously described (78). Anesthesized rats, with a cannulated tail
608 vein (with a 0.020" ×0.060" OD Tygon microbore tubing, 45 cm long and a 25 gauge needle) were
609 placed in a combined MRI/PET system, comprising a Bruker AV4 70/30 BioSpec MRI including a 7T,
610 300 mm bore magnet with B-GA20S HP gradients and operating with Paravision 360 V3.5. The PET
611 images are acquired on a 3-ring PET insert with an axial FOV of 150mm, transaxial FOV of 80 mm. A
612 40 mm ID rat head MRI rf coil inside the PET ring was used to acquire head images simultaneously
613 with the PET acquisition. A 60 min PET and dynamic GE images with 200 repetitions were started
614 simultaneously. After approximately 2 min of scanning the rats were injected with approximately 30
615 MBq of PET tracer solution, 300 µl Gadovist and saline/10% ethanol to give a total volume of 400µl.
616 This volume was injected manually via the catheter inserted into the tail vein in a slow bolus injection.
617 Following 12 min of dynamic GE scanning, the following MR scanning was performed during the PET
618 acquisition:

619 PET reconstruction was performed using OSEM 0.5 with iterations = 1, Scatter correction, Randoms
620 correction, Decay correction, Partial volume correction, point spread function correction, attenuation
621 correction generated from the 3D FISP 250 µm coronal sequence and partitioning of 10 x 60 sec and
622 10 x 300 sec time frames. The dynamic PET series were then geometrically registered to the T2
623 turboRARE transverse image set and the 3D FISP 250 µm image set. PET/MR data were analysed using
624 the PMOD software. PET and MR data for each animal were matched, registered onto the Schiffer rat
625 brain atlas and segmented (116). SUV/BW values were calculated after normalizing for decay and
626 bodyweight of each animal scanned.

627 *Molecular profiling and RNAseq of brain regions and Kidney*

628 Brain tissue from one hemisphere was minced and snap frozen. RNA was extracted using TRIzol
629 reagent using standard manufacturer's protocol. 1μg of RNA was used to synthesize cDNA according
630 to manufacturer's protocol (Meridian bioscience). qRT-PCR was performed with 2x SYBR green
631 reagent (Thermofisher) with the primer sequences (56). Cortex, hippocampus, and thalamus were
632 sampled using a biopsy punch (1mm diameter) and placed directly into TRIzol and RNA extracted.
633 Whole kidneys were snap frozen at collection and RNA extracted using TRIzol reagent.

634 Library preparation and sequencing was performed at the University of Queensland Sequencing
635 Facility (University of Queensland, Brisbane, Australia). Bar-coded RNA-Sequencing (RNA-Seq)
636 libraries were generated using the Illumina Stranded mRNA Library Prep Ligation kit (Illumina, CA,
637 USA) and IDT for Illumina RNA UD Indexes (Illumina, CA, USA). The bar coded RNA libraries were
638 pooled in equimolar ratios prior to sequencing using the Illumina NovaSeq 6000 (Illumina, CA, USA).
639 Paired-end 102 bp reads were generated using either a NovaSeq S2 reagent kit v1.5 (200 cycles)
640 (Illumina, CA, USA). After sequencing, fastq files were created using bcl2fastq2 (v2.20.0.422). Raw
641 sequencing data (in the form of .fastq files) was provided by the sequencing facility for further analysis.
642 Raw reads were pre-processed using fastp v0.23.2 using previously described parameters (52, 117)
643 FastQC was used on pre and post-trimmed reads to ensure adequate sequence quality, GC content,
644 and removal of adapter sequences (118).

645 The reference transcriptome used in this study was created by combining the unique protein-coding
646 transcripts from the Ensembl and NCBI RefSeq databases of the Rnor6.0 annotation, as previously
647 described (55). After pre-processing, transcript expression level was quantified as transcripts per
648 million using Kallisto (v0.46.0).(119) Kallisto expression files were imported into RStudio (R version
649 4.2.1) using the tximport package (v1.24.0) to collate transcript-level TPM generated by Kallisto into
650 gene-level TPMs for use by downstream tools.

651 All network cluster analysis was based on gene-level expression and was conducted using Graphia
652 (https://graphia.app) (120). Only genes expressed at ≥ 1 TPM in at least 2 samples were retained for

analysis. A network graph was then created where nodes (genes) were connected by edges (representing correlation coefficients). Relationships where $r \geq 0.85$ were included. Samples which exhibited similar patterns of gene expression across tissues were placed close together in the network graph. Gene expression patterns were further characterised using the Markov Cluster Algorithm (MCL) with an inflation value of 2.0 to identify clusters of transcripts with similar expression patterns.

Statistics

All data are presented as mean ± standard deviation and analysed with Graphpad Prism (9.0 or 10.0). Statistical testing was performed using an ANOVA with Tukey post-hoc analysis or t-test for pairwise comparisons. P values <0.05 are considered significant. Statistical analysis for DPA-714-F18 uptake were undertaken using R version 4.4.1. Data was analysed using linear regression to assess the association between SUV-BW and genotype as the main predictor, sex and age cohort and the interactions between these three variables where appropriate. Hierarchical model building was employed to determine the best fit model for each region of the brain.

Data availability

All data are provided in supplemental file. Sequencing data can be accessed through accession number

669 References

670 1. Cox N, Pokrovskii M, Vicario R, and Geissmann F. Origins, Biology, and Diseases of Tissue
671 Macrophages. *Annu Rev Immunol.* 2021;39:313-44.
672 2. Hume DA, Irvine KM, and Pridans C. The Mononuclear Phagocyte System: The Relationship
673 between Monocytes and Macrophages. *Trends Immunol.* 2019;40(2):98-112.
674 3. Jenkins SJ, and Allen JE. The expanding world of tissue-resident macrophages. *Eur J Immunol.*
675 2021;51(8):1882-96.
676 4. Lazarov T, Juarez-Carreno S, Cox N, and Geissmann F. Physiology and diseases of tissue-
677 resident macrophages. *Nature.* 2023;618(7966):698-707.
678 5. Mass E, Nimmerjahn F, Kierdorf K, and Schlitzer A. Tissue-specific macrophages: how they
679 develop and choreograph tissue biology. *Nat Rev Immunol.* 2023;23(9):563-79.
680 6. Grabert K, Sehgal A, Irvine KM, Wollscheid-Lengeling E, Ozdemir DD, Stables J, et al. A
681 Transgenic Line That Reports CSF1R Protein Expression Provides a Definitive Marker for the
682 Mouse Mononuclear Phagocyte System. *J Immunol.* 2020;205(11):3154-66.
683 7. Chitu V, and Stanley ER. Regulation of Embryonic and Postnatal Development by the CSF-1
684 Receptor. *Curr Top Dev Biol.* 2017;123:229-75.
685 8. Hume DA, Caruso M, Ferrari-Cestari M, Summers KM, Pridans C, and Irvine KM. Phenotypic
686 impacts of CSF1R deficiencies in humans and model organisms. *J Leukoc Biol.*
687 2020;107(2):205-19.
688 9. MacDonald KP, Palmer JS, Cronau S, Seppanen E, Olver S, Raffelt NC, et al. An antibody
689 against the colony-stimulating factor 1 receptor depletes the resident subset of monocytes
690 and tissue- and tumor-associated macrophages but does not inhibit inflammation. *Blood.*
691 2010;116(19):3955-63.
692 10. Cecchini MG, Dominguez MG, Mocci S, Wetterwald A, Felix R, Fleisch H, et al. Role of colony
693 stimulating factor-1 in the establishment and regulation of tissue macrophages during
694 postnatal development of the mouse. *Development.* 1994;120(6):1357-72.
695 11. Van Wesenbeeck L, Odgren PR, MacKay CA, D'Angelo M, Safadi FF, Popoff SN, et al. The
696 osteopetrotic mutation toothless (tl) is a loss-of-function frameshift mutation in the rat Csf1
697 gene: Evidence of a crucial role for CSF-1 in osteoclastogenesis and endochondral
698 ossification. *Proc Natl Acad Sci U S A.* 2002;99(22):14303-8.
699 12. Dai XM, Ryan GR, Hapel AJ, Dominguez MG, Russell RG, Kapp S, et al. Targeted disruption of
700 the mouse colony-stimulating factor 1 receptor gene results in osteopetrosis, mononuclear
701 phagocyte deficiency, increased primitive progenitor cell frequencies, and reproductive
702 defects. *Blood.* 2002;99(1):111-20.
703 13. Lin H, Lee E, Hestir K, Leo C, Huang M, Bosch E, et al. Discovery of a cytokine and its receptor
704 by functional screening of the extracellular proteome. *Science.* 2008;320(5877):807-11.
705 14. Garceau V, Smith J, Paton IR, Davey M, Fares MA, Sester DP, et al. Pivotal Advance: Avian
706 colony-stimulating factor 1 (CSF-1), interleukin-34 (IL-34), and CSF-1 receptor genes and
707 gene products. *J Leukoc Biol.* 2010;87(5):753-64.
708 15. Hume DA, Gutowska-Ding MW, Garcia-Morales C, Kebede A, Bamidele O, Trujillo AV, et al.
709 Functional evolution of the colony-stimulating factor 1 receptor (CSF1R) and its ligands in
710 birds. *J Leukoc Biol.* 2020;107(2):237-50.
711 16. Kuil LE, Oosterhof N, Geurts SN, van der Linde HC, Meijering E, and van Ham TJ. Reverse
712 genetic screen reveals that Il34 facilitates yolk sac macrophage distribution and seeding of
713 the brain. *Dis Model Mech.* 2019;12(3):dmm037762.
714 17. Wang T, Kono T, Monte MM, Kuse H, Costa MM, Korenaga H, et al. Identification of IL-34 in
715 teleost fish: differential expression of rainbow trout IL-34, MCSF1 and MCSF2, ligands of the
716 MCSF receptor. *Mol Immunol.* 2013;53(4):398-409.
717 18. Wu S, Xue R, Hassan S, Nguyen TML, Wang T, Pan H, et al. Il34-Csf1r Pathway Regulates the
718 Migration and Colonization of Microglial Precursors. *Dev Cell.* 2018;46(5):552-63 e4.

19. Yu T, Kuang H, Wu X, Huang Y, Wang J, and Wen Z. Cell competition for neuron-derived trophic factor controls the turnover and lifespan of microglia. *Sci Adv.* 2023;9(24):eadf9790.
20. Ma X, Lin WY, Chen Y, Stawicki S, Mukhyala K, Wu Y, et al. Structural basis for the dual recognition of helical cytokines IL-34 and CSF-1 by CSF-1R. *Structure.* 2012;20(4):676-87.
21. Lelios I, Cansever D, Utz SG, Mildenberger W, Stifter SA, and Greter M. Emerging roles of IL-34 in health and disease. *J Exp Med.* 2020;217(3):e20190290.
22. Wei S, Nandi S, Chitu V, Yeung YG, Yu W, Huang M, et al. Functional overlap but differential expression of CSF-1 and IL-34 in their CSF-1 receptor-mediated regulation of myeloid cells. *J Leukoc Biol.* 2010;88(3):495-505.
23. Greter M, Lelios I, Pelczar P, Hoeffel G, Price J, Leboeuf M, et al. Stroma-derived interleukin-34 controls the development and maintenance of langerhans cells and the maintenance of microglia. *Immunity.* 2012;37(6):1050-60.
24. Wang Y, Szretter KJ, Vermi W, Gilfillan S, Rossini C, Cella M, et al. IL-34 is a tissue-restricted ligand of CSF1R required for the development of Langerhans cells and microglia. *Nat Immunol.* 2012;13(8):753-60.
25. Nandi S, Gokhan S, Dai XM, Wei S, Enikolopov G, Lin H, et al. The CSF-1 receptor ligands IL-34 and CSF-1 exhibit distinct developmental brain expression patterns and regulate neural progenitor cell maintenance and maturation. *Dev Biol.* 2012;367(2):100-13.
26. Easley-Neal C, Foreman O, Sharma N, Zarrin AA, and Weimer RM. CSF1R Ligands IL-34 and CSF1 Are Differentially Required for Microglia Development and Maintenance in White and Gray Matter Brain Regions. *Front Immunol.* 2019;10:2199.
27. Kana V, Desland FA, Casanova-Acebes M, Ayata P, Badimon A, Nabel E, et al. CSF-1 controls cerebellar microglia and is required for motor function and social interaction. *J Exp Med.* 2019;216(10):2265-81.
28. Nandi S, Cioce M, Yeung YG, Nieves E, Tesfa L, Lin H, et al. Receptor-type protein-tyrosine phosphatase zeta is a functional receptor for interleukin-34. *J Biol Chem.* 2013;288(30):21972-86.
29. Segaliny AI, Brion R, Mortier E, Maillasson M, Cherel M, Jacques Y, et al. Syndecan-1 regulates the biological activities of interleukin-34. *Biochim Biophys Acta.* 2015;1853(5):1010-21.
30. Xie X, Zhang W, Xiao M, Wei T, Qiu Y, Qiu J, et al. TREM2 acts as a receptor for IL-34 to suppress acute myeloid leukemia in mice. *Blood.* 2023;141(26):3184-98.
31. Abdel-Rehim AS, Mohamed NA, and Shakweer MM. Interleukin-34 as a marker for subclinical proliferative lupus nephritis. *Lupus.* 2020;29(6):607-16.
32. Baghdadi M, Umeyama Y, Hama N, Kobayashi T, Han N, Wada H, and Seino KI. Interleukin-34, a comprehensive review. *J Leukoc Biol.* 2018;104(5):931-51.
33. Franze E, Laudisi F, Di Grazia A, Maronek M, Bellato V, Sica G, and Monteleone G. Macrophages produce and functionally respond to interleukin-34 in colon cancer. *Cell Death Discov.* 2020;6(1):117.
34. Franze E, Monteleone I, Cupi ML, Mancia P, Caprioli F, Marafini I, et al. Interleukin-34 sustains inflammatory pathways in the gut. *Clin Sci (Lond).* 2015;129(3):271-80.
35. Franze E, Stolfi C, Troncone E, Scarozza P, and Monteleone G. Role of Interleukin-34 in Cancer. *Cancers (Basel).* 2020;12(1):252.
36. Kashiwagi M, Ozaki Y, Imanishi T, Taruya A, Kuroi A, Katayama Y, et al. Interleukin-34 levels are increased in acute myocardial infarction and associated with major adverse cardiovascular events. *Coron Artery Dis.* 2022;31(1):61-3.
37. Liu Y, Zhang B, Lei Y, Xia L, Lu J, and Shen H. Serum levels of interleukin-34 and clinical correlation in patients with primary Sjogren's syndrome. *Int J Rheum Dis.* 2020;23(3):374-80.
38. Masteller EL, and Wong BR. Targeting IL-34 in chronic inflammation. *Drug Discov Today.* 2014;19(8):1212-6.

39. Munoz-Garcia J, Cochonneau D, Teletchea S, Moranton E, Lanoe D, Brion R, et al. The twin cytokines interleukin-34 and CSF-1: masterful conductors of macrophage homeostasis. *Theranostics.* 2021;11(4):1568-93.
40. Nakamichi Y, Udagawa N, and Takahashi N. IL-34 and CSF-1: similarities and differences. *J Bone Miner Metab.* 2013;31(5):486-95.
41. Otsuka R, Wada H, and Seino KI. IL-34, the rationale for its expression in physiological and pathological conditions. *Semin Immunol.* 2021;54:101517.
42. Shang J, Xu Y, Pu S, Sun X, and Gao X. Role of IL-34 and its receptors in inflammatory diseases. *Cytokine.* 2023;171:156348.
43. Zwicker S, Martinez GL, Bosma M, Gerling M, Clark R, Majster M, et al. Interleukin 34: a new modulator of human and experimental inflammatory bowel disease. *Clin Sci (Lond).* 2015;129(3):281-90.
44. Bezie S, Freuchet A, Serazin C, Salama A, Vimond N, Anegon I, and Guillonneau C. IL-34 Actions on FOXP3(+) Tregs and CD14(+) Monocytes Control Human Graft Rejection. *Front Immunol.* 2020;11:1496.
45. Bezie S, Picarda E, Ossart J, Tesson L, Usal C, Renaudin K, et al. IL-34 is a Treg-specific cytokine and mediates transplant tolerance. *J Clin Invest.* 2015;125(10):3952-64.
46. Baek JH, Zeng R, Weinmann-Menke J, Valerius MT, Wada Y, Ajay AK, et al. IL-34 mediates acute kidney injury and worsens subsequent chronic kidney disease. *J Clin Invest.* 2015;125(8):3198-214.
47. Wada Y, Gonzalez-Sanchez HM, Weinmann-Menke J, Iwata Y, Ajay AK, Meineck M, and Kelley VR. IL-34-Dependent Intrarenal and Systemic Mechanisms Promote Lupus Nephritis in MRL-Fas(lpr) Mice. *J Am Soc Nephrol.* 2019;30(2):244-59.
48. Isbel NM, Hill PA, Foti R, Mu W, Hurst LA, Stambe C, et al. Tubules are the major site of M-CSF production in experimental kidney disease: correlation with local macrophage proliferation. *Kidney Int.* 2001;60(2):614-25.
49. Le Meur Y, Tesch GH, Hill PA, Mu W, Foti R, Nikolic-Paterson DJ, and Atkins RC. Macrophage accumulation at a site of renal inflammation is dependent on the M-CSF/c-fms pathway. *J Leukoc Biol.* 2002;72(3):530-7.
50. Alikhan MA, Jones CV, Williams TM, Beckhouse AG, Fletcher AL, Kett MM, et al. Colony-stimulating factor-1 promotes kidney growth and repair via alteration of macrophage responses. *Am J Pathol.* 2011;179(3):1243-56.
51. Hume DA, Caruso M, Keshvari S, Patkar OL, Sehgal A, Bush SJ, et al. The Mononuclear Phagocyte System of the Rat. *J Immunol.* 2021;206(10):2251-63.
52. Keshvari S, Caruso M, Teakle N, Batoon L, Sehgal A, Patkar OL, et al. CSF1R-dependent macrophages control postnatal somatic growth and organ maturation. *PLoS Genet.* 2021;17(6):e1009605.
53. Pridans C, Raper A, Davis GM, Alves J, Sauter KA, Lefevre L, et al. Pleiotropic Impacts of Macrophage and Microglial Deficiency on Development in Rats with Targeted Mutation of the Csf1r Locus. *J Immunol.* 2018;201(9):2683-99.
54. Consortium F, the RP, Clst, Forrest AR, Kawaji H, Rehli M, et al. A promoter-level mammalian expression atlas. *Nature.* 2014;507(7493):462-70.
55. Summers KM, Bush SJ, Wu C, and Hume DA. Generation and network analysis of an RNA-seq transcriptional atlas for the rat. *NAR Genom Bioinform.* 2022;4(1):lqac017.
56. Carter-Cusack D, Huang S, Keshvari S, Patkar O, Sehgal A, Allavena R, et al. Wild-type bone marrow cells repopulate tissue resident macrophages and reverse the impacts of homozygous CSF1R mutation. *PLoS Genetics.* 2024:In press.
57. Freuchet A, Salama A, Bezie S, Tesson L, Remy S, Humeau R, et al. IL-34 deficiency impairs FOXP3(+) Treg function in a model of autoimmune colitis and decreases immune tolerance homeostasis. *Clin Transl Med.* 2022;12(8):e988.

58. Irvine KM, Caruso M, Cestari MF, Davis GM, Keshvari S, Sehgal A, et al. Analysis of the impact of CSF-1 administration in adult rats using a novel Csf1r-mApple reporter gene. *J Leukoc Biol.* 2020;107(2):221-35.
59. Sehgal A, Carter-Cusack D, Keshvari S, Patkar O, Huang S, Summers KM, et al. Intraperitoneal transfer of wild-type bone marrow repopulates tissue macrophages in the Csf1r knockout rat without contributing to monocytopoiesis. *Eur J Immunol.* 2023;53(8):e2250312.
60. Wang Y, and Colonna M. Interkeukin-34, a cytokine crucial for the differentiation and maintenance of tissue resident macrophages and Langerhans cells. *Eur J Immunol.* 2014;44(6):1575-81.
61. Gu X, Heinrich A, Li SY, and DeFalco T. Testicular macrophages are recruited during a narrow fetal time window and promote organ-specific developmental functions. *Nat Commun.* 2023;14(1):1439.
62. Mossadegh-Keller N, Gentek R, Gimenez G, Bigot S, Mailfert S, and Sieweke MH. Developmental origin and maintenance of distinct testicular macrophage populations. *J Exp Med.* 2017;214(10):2829-41.
63. Mossadegh-Keller N, and Sieweke MH. Characterization of Mouse Adult Testicular Macrophage Populations by Immunofluorescence Imaging and Flow Cytometry. *Bio Protoc.* 2019;9(5):e3178.
64. Paolicelli RC, Sierra A, Stevens B, Tremblay ME, Aguzzi A, Ajami B, et al. Microglia states and nomenclature: A field at its crossroads. *Neuron.* 2022;110(21):3458-83.
65. Zhang Z, Zhang ZY, Wu Y, and Schluesener HJ. Lesional accumulation of CD163+ macrophages/microglia in rat traumatic brain injury. *Brain Res.* 2012;1461:102-10.
66. Patkar OL, Caruso M, Teakle N, Keshvari S, Bush SJ, Pridans C, et al. Analysis of homozygous and heterozygous Csf1r knockout in the rat as a model for understanding microglial function in brain development and the impacts of human CSF1R mutations. *Neurobiol Dis.* 2021;151:105268.
67. Devlin BA, Nguyen DM, Grullon G, Clark MJ, Ceasrine AM, Deja M, et al. Neuron Derived Cytokine Interleukin-34 Controls Developmental Microglia Function. *bioRxiv.* 2024;2024:2024.05.10.589920.
68. Buttgereit A, Lelios I, Yu X, Vrohlings M, Krakoski NR, Gautier EL, et al. Sall1 is a transcriptional regulator defining microglia identity and function. *Nat Immunol.* 2016;17(12):1397-406.
69. Fixsen BR, Han CZ, Zhou Y, Spann NJ, Saisan P, Shen Z, et al. SALL1 enforces microglia-specific DNA binding and function of SMADs to establish microglia identity. *Nat Immunol.* 2023;24(7):1188-99.
70. Dulski J, Muthusamy K, Lund TC, and Wszolek ZK. CSF1R-related disorder: State of the art, challenges, and proposition of a new terminology. *Parkinsonism Relat Disord.* 2024;121:105894.
71. Ellenbroek B, and Youn J. Rodent models in neuroscience research: is it a rat race? *Dis Model Mech.* 2016;9(10):1079-87.
72. Bradford BM, McGuire LI, Hume DA, Pridans C, and Mabbott NA. Microglia deficiency accelerates prion disease but does not enhance prion accumulation in the brain. *Glia.* 2022;70(11):2169-87.
73. Kiani Shabestari S, Morabito S, Danhash EP, McQuade A, Sanchez JR, Miyoshi E, et al. Absence of microglia promotes diverse pathologies and early lethality in Alzheimer's disease mice. *Cell Rep.* 2022;39(11):110961.
74. Vicidomini C, Panico M, Greco A, Gargiulo S, Coda AR, Zannetti A, et al. In vivo imaging and characterization of [(18)F]DPA-714, a potential new TSPO ligand, in mouse brain and peripheral tissues using small-animal PET. *Nucl Med Biol.* 2015;42(3):309-16.

868 75. Alam MM, Lee J, and Lee SY. Recent Progress in the Development of TSPO PET Ligands for
869 Neuroinflammation Imaging in Neurological Diseases. *Nucl Med Mol Imaging.*
870 2017;51(4):283-96.
871 76. Crawshaw AA, and Robertson NP. The role of TSPO PET in assessing neuroinflammation. *J*
872 *Neurol.* 2017;264(8):1825-7.
873 77. Guilarte TR, Rodichkin AN, McGlothan JL, Acanda De La Rocha AM, and Azzam DJ. Imaging
874 neuroinflammation with TSPO: A new perspective on the cellular sources and subcellular
875 localization. *Pharmacol Ther.* 2022;234:108048.
876 78. James ML, Fulton RR, Vercoullie J, Henderson DJ, Garreau L, Chalon S, et al. DPA-714, a new
877 translocator protein-specific ligand: synthesis, radiofluorination, and pharmacologic
878 characterization. *J Nucl Med.* 2008;49(5):814-22.
879 79. Golla SS, Boellaard R, Oikonen V, Hoffmann A, van Berckel BN, Windhorst AD, et al.
880 Quantification of [18F]DPA-714 binding in the human brain: initial studies in healthy controls
881 and Alzheimer's disease patients. *J Cereb Blood Flow Metab.* 2015;35(5):766-72.
882 80. Peyronneau MA, Kuhnast B, Nguyen DL, Jego B, Sayet G, Caille F, et al. [(18)F]DPA-714: Effect
883 of co-medications, age, sex, BMI and TSPO polymorphism on the human plasma input
884 function. *Eur J Nucl Med Mol Imaging.* 2023;50(11):3251-64.
885 81. Arreola MA, Soni N, Crapser JD, Hohsfield LA, Elmore MRP, Matheos DP, et al. Microglial
886 dyshomeostasis drives perineuronal net and synaptic loss in a CSF1R(+/-) mouse model of
887 ALSP, which can be rescued via CSF1R inhibitors. *Sci Adv.* 2021;7(35):eabg1601.
888 82. Crapser JD, Spangenberg EE, Barahona RA, Arreola MA, Hohsfield LA, and Green KN.
889 Microglia facilitate loss of perineuronal nets in the Alzheimer's disease brain. *EBioMedicine.*
890 2020;58:102919.
891 83. Chadarevian JP, Hasselmann J, Lahian A, Capocchi JK, Escobar A, Lim TE, et al. Therapeutic
892 potential of human microglia transplantation in a chimeric model of CSF1R-related
893 leukoencephalopathy. *Neuron.* 2024;112(16):2686-707 e8.
894 84. Munro DAD, Bestard-Cuche N, McQuade A, Chagnot A, Kiani Shabestari S, Chadarevian JP, et
895 al. Microglia provide resilience against region-selective neuropathology with ageing. *Neuron.*
896 2024;In press.
897 85. Diwan V, Brown L, and Gobe GC. Adenine-induced chronic kidney disease in rats. *Nephrology*
898 *(Carlton).* 2018;23(1):5-11.
899 86. Diwan V, Small D, Kauter K, Gobe GC, and Brown L. Gender differences in adenine-induced
900 chronic kidney disease and cardiovascular complications in rats. *Am J Physiol Renal Physiol.*
901 2014;307(11):F1169-78.
902 87. Cantero-Navarro E, Rayego-Mateos S, Orejudo M, Tejedor-Santamaria L, Tejera-Munoz A,
903 Sanz AB, et al. Role of Macrophages and Related Cytokines in Kidney Disease. *Front Med*
904 *(Lausanne).* 2021;8:688060.
905 88. Giotti B, Chen SH, Barnett MW, Regan T, Ly T, Wiemann S, et al. Assembly of a parts list of
906 the human mitotic cell cycle machinery. *J Mol Cell Biol.* 2019;11(8):703-18.
907 89. Summers KM, Bush SJ, and Hume DA. Network analysis of transcriptomic diversity amongst
908 resident tissue macrophages and dendritic cells in the mouse mononuclear phagocyte
909 system. *PLoS Biol.* 2020;18(10):e3000859.
910 90. Djudjaj S, Papasotiriou M, Bulow RD, Wagnerova A, Lindenmeyer MT, Cohen CD, et al.
911 Keratins are novel markers of renal epithelial cell injury. *Kidney Int.* 2016;89(4):792-808.
912 91. Wozniak J, Floege J, Ostendorf T, and Ludwig A. Key metalloproteinase-mediated pathways
913 in the kidney. *Nat Rev Nephrol.* 2021;17(8):513-27.
914 92. Pap D, Veres-Szekely A, Szebeni B, Rokonay R, Onody A, Lippai R, et al. Characterization of IL-
915 19, -20, and -24 in acute and chronic kidney diseases reveals a pro-fibrotic role of IL-24. *J*
916 *Transl Med.* 2020;18(1):172.

917 93. Schutte-Nutgen K, Edeling M, Kentrup D, Heitplatz B, Van Marck V, Zarbock A, et al.
918 Interleukin 24 promotes cell death in renal epithelial cells and is associated with acute renal
919 injury. *Am J Transplant.* 2022;22(11):2548-59.
920 94. Ludwig-Portugall I, Bartok E, Dhana E, Evers BD, Primiano MJ, Hall JP, et al. An NLRP3-specific
921 inflammasome inhibitor attenuates crystal-induced kidney fibrosis in mice. *Kidney Int.*
922 2016;90(3):525-39.
923 95. Bhairavabhotla R, Kim YC, Glass DD, Escobar TM, Patel MC, Zahr R, et al. Transcriptome
924 profiling of human FoxP3+ regulatory T cells. *Hum Immunol.* 2016;77(2):201-13.
925 96. Luo Y, Xu C, Wang B, Niu Q, Su X, Bai Y, et al. Single-cell transcriptomic analysis reveals
926 disparate effector differentiation pathways in human T(reg) compartment. *Nat Commun.*
927 2021;12(1):3913.
928 97. Menoret S, Tesson L, Remy S, Gourain V, Serazin C, Usal C, et al. CD4(+) and CD8(+)
929 regulatory T cell characterization in the rat using a unique transgenic Foxp3-EGFP model.
930 *BMC Biol.* 2023;21(1):8.
931 98. Lawson LJ, Perry VH, Dri P, and Gordon S. Heterogeneity in the distribution and morphology
932 of microglia in the normal adult mouse brain. *Neuroscience.* 1990;39(1):151-70.
933 99. Askew K, Li K, Olmos-Alonso A, Garcia-Moreno F, Liang Y, Richardson P, et al. Coupled
934 Proliferation and Apoptosis Maintain the Rapid Turnover of Microglia in the Adult Brain. *Cell*
935 *Rep.* 2017;18(2):391-405.
936 100. Stables J, Green EK, Sehgal A, Patkar OL, Keshvari S, Taylor I, et al. A kinase-dead Csf1r
937 mutation associated with adult-onset leukoencephalopathy has a dominant inhibitory
938 impact on CSF1R signalling. *Development.* 2022;149(8):dev200237.
939 101. Sehgal A, Irvine KM, and Hume DA. Functions of macrophage colony-stimulating factor
940 (CSF1) in development, homeostasis, and tissue repair. *Semin Immunol.* 2021;54:101509.
941 102. McNamara NB, Munro DAD, Bestard-Cuche N, Uyeda A, Bogie JFJ, Hoffmann A, et al.
942 Microglia regulate central nervous system myelin growth and integrity. *Nature.*
943 2023;613(7942):120-9.
944 103. Liu YJ, Spangenberg EE, Tang B, Holmes TC, Green KN, and Xu X. Microglia Elimination
945 Increases Neural Circuit Connectivity and Activity in Adult Mouse Cortex. *J Neurosci.*
946 2021;41(6):1274-87.
947 104. O'Keeffe M, Sam Booker, Darren Walsh, Mosi Li, Chloe Henley, Laura Simoes de Oliveira, et
948 al. Typical development of synaptic and neuronal properties can proceed without microglia.
949 *Biorxiv.* 2024:2024.09. 06.611614.
950 105. Berglund R, Cheng Y, Piket E, M ZA, Zeitelhofer M, Olsson T, et al. The aging mouse CNS is
951 protected by an autophagy-dependent microglia population promoted by IL-34. *Nat*
952 *Commun.* 2024;15(1):383.
953 106. de Rojas I, Moreno-Grau S, Tesi N, Grenier-Boley B, Andrade V, Jansen IE, et al. Common
954 variants in Alzheimer's disease and risk stratification by polygenic risk scores. *Nat Commun.*
955 2021;12(1):3417.
956 107. Rogers NM, Ferenbach DA, Isenberg JS, Thomson AW, and Hughes J. Dendritic cells and
957 macrophages in the kidney: a spectrum of good and evil. *Nat Rev Nephrol.* 2014;10(11):625-
958 43.
959 108. Liu ZX, Chen WJ, Wang Y, Chen BQ, Liu YC, Cheng TC, et al. Interleukin-34 deficiency
960 aggravates development of colitis and colitis-associated cancer in mice. *World J*
961 *Gastroenterol.* 2022;28(47):6752-68.
962 109. Batoon L, Keshvari S, Irvine KM, Ho E, Caruso M, Patkar OL, et al. Relative contributions of
963 osteal macrophages and osteoclasts to postnatal bone development in CSF1R-deficient rats
964 and phenotype rescue following wild-type bone marrow cell transfer. *J Leukoc Biol.* 2024.
965 110. Huang S, Carter-Cusack D, Maxwell E, Patkar OL, Irvine KM, and Hume DA. Genetic and
966 Immunohistochemistry Tools to Visualize Rat Macrophages In Situ. *Methods Mol Biol.*
967 2024;2713:99-115.

968 111. Stewart AW, Robinson SD, O'Brien K, Jin J, Widhalm G, Hangel G, et al. QSMxT: Robust
969 masking and artifact reduction for quantitative susceptibility mapping. *Magn Reson Med.*
970 2022;87(3):1289-300.
971 112. Avants BB, Tustison NJ, Song G, Cook PA, Klein A, and Gee JC. A reproducible evaluation of
972 ANTs similarity metric performance in brain image registration. *Neuroimage.*
973 2011;54(3):2033-44.
974 113. Johnson GA, Calabrese E, Badea A, Paxinos G, and Watson C. A multidimensional magnetic
975 resonance histology atlas of the Wistar rat brain. *Neuroimage.* 2012;62(3):1848-56.
976 114. Papp EA, Leergaard TB, Calabrese E, Johnson GA, and Bjaalie JG. Waxholm Space atlas of the
977 Sprague Dawley rat brain. *Neuroimage.* 2014;97:374-86.
978 115. Calamante F, Tournier JD, Kurniawan ND, Yang Z, Gyengesi E, Galloway GJ, et al. Super-
979 resolution track-density imaging studies of mouse brain: comparison to histology.
980 *Neuroimage.* 2012;59(1):286-96.
981 116. Schiffer WK, Mirrione MM, Biegon A, Alexoff DL, Patel V, and Dewey SL. Serial microPET
982 measures of the metabolic reaction to a microdialysis probe implant. *J Neurosci Methods.*
983 2006;155(2):272-84.
984 117. Chen S, Zhou Y, Chen Y, and Gu J. fastp: an ultra-fast all-in-one FASTQ preprocessor.
985 *Bioinformatics.* 2018;34(17):i884-i90.
986 118. Wingett SW, and Andrews S. FastQ Screen: A tool for multi-genome mapping and quality
987 control. *F1000Res.* 2018;7:1338.
988 119. Bray NL, Pimentel H, Melsted P, and Pachter L. Near-optimal probabilistic RNA-seq
989 quantification. *Nat Biotechnol.* 2016;34(5):525-7.
990 120. Freeman TC, Horsewell S, Patir A, Harling-Lee J, Regan T, Shih BB, et al. Graphia: A platform
991 for the graph-based visualisation and analysis of high dimensional data. *PLoS Comput Biol.*
992 2022;18(7):e1010310.

993

994 **Legends to Figures**

995 **Figure 1. *Il34* is widely-expressed in rat tissues but is not required for normal growth and**
996 **development.**

997 **(A)** The image shows mapping of RNA-seq reads from the rat atlas to the *Il34* locus. Each dot
998 represents read count from an individual tissue/library, colour coded based upon system as indicated.
999 The location on Chr19 (mRatBN7.2 assembly) is shown on the x axis*; Il34* is transcribed on the reverse
1000 strand; the first coding exon at 38.729Mb is detected in libraries from all tissues (CDS exon 1). An
1001 alternative non-coding exon at ca. 38.753Mb is detected primarily in libraries from mesenchymal
1002 tissues (respiratory, cardiovascular, renal). The most distal 5' non-coding exon, at 38.764Mb, is
1003 detected at low levels in multiple tissues. To the right of the image, reads are mapped to exons of the
1004 upstream *Sf3b3* locus.

1005 **(B)** Tibial bone density was measured by microCT in male and female rats at 8 weeks of age (BV/TV;
1006 Bone volume fraction, Tb.Th; trabecular thickness, Tb.N; trabecular number, TV; Total volume, Cort.
1007 Th; Cortical Thickness). Each dot represents an individual animal (n≥4).

1008 **(C)** Body weight gain. WT (blue) and *Il34*$^{-/-}$ (grey) rats were weighed when ear-notched (P12/P14), at
1009 weaning (P20/P21) and at P56. Each dot represents an independent animal.

1010 **(D&E)** Representative images of spleen morphology and distribution of macrophages in *Il34*$^{+/+}$ (upper
1011 panels) and *Il34*$^{-/-}$ (lower panels) rats. IBA1 staining (left) highlights the macrophages of the red pulp;
1012 and CD209b (right) the marginal zone macrophages.

1013 **(F)** Serum CSF1 was measured by ELISA. Each dot represents an individual animal.

1014 **(G)** Flow cytometric analysis of CD45R^{+} B and CD3^{+} T cells, granulocytes, HIS48^{+}(classical) and
1015 CD43^{+}(non-classical) monocytes from bone marrow, blood and spleen in 8 week old rats (n≥6). **(H)** *Ex*
1016 *vivo* imaging of diaphragm muscle and central tendon and the thymus isolated from *Il34*$^{+/+}$ and *Il34*$^{-/-}$
1017 animals carrying the *Csf1r*-mApple transgene. Tissues were directly imaged on an Olympus FV3000
1018 confocal microscope with a 10x objective and scalebar represents 100 μM.

1019 **Figure 2. Loss of IL34 reduces tissue resident macrophages in squamous epithelia and brain.**

1020 **(A)** Whole mount imaging of the epithelial layer of the ear, tongue, proximal oesophagus and foot
1021 from *Il34*$^{+/+}$ and *Il34*$^{-/-}$ animals carrying the *Csf1r*-mApple transgene. **(B)** Whole mount imaging of the
1022 mesothelium (surface), peritubular and interstitial regions of the testes. Tissues were directly imaged
1023 on an Olympus FV3000 confocal microscope with a 10x objective and scalebar represents 100 μM. **(C)**
1024 Half brains from *Il34*$^{+/+}$, *Il34*$^{+/-}$ and *Il34*$^{-/-}$ animals with the *Csf1r*-mApple reporter were homogenized
1025 into single cell suspension and analysed by flow cytometry. Total cells were enumerated after
1026 extraction and total numbers of microglia (CD45^{low}/Cd11b/c^{high}) and brain associated macrophages
1027 (BAM; CD45^{high}/CD11b/c^{low}) were calculated from proportions derived from flow cytometry.
1028 Representative plots from each genotype are shown and quantified, each dot represents an
1029 independent animal (n≥12).

1030 **Figure 3. Loss of IL34 leads to selective reduction of microglia in grey matter regions**

1031 **(A)** Representative images of brain sections stained for IBA1 (Green or Red) and DAPI (Blue) Images
1032 were captured on the Olympus FV3000 confocal microscope. Grey matter in cerebellum is demarcated
1033 by white dashed line. **(B)** Microglial density for each brain region (specifically grey matter in
1034 cerebellum) was quantified as described in Materials and Methods. Each point represents data from
1035 an individual animal. Statistical analysis was performed using a One-way ANOVA.

1036 **Figure 4. A gradient of microglial density and selective depletion of perivascular macrophages in**
1037 **grey matter of IL34-deficient rats**

1038 **(A)** Free floating sections of cortex from *Il34*$^{+/+}$, *Il34*$^{+/-}$ and *Il34*$^{-/-}$ brains stained with IBA1 (green) and
1039 DAPI (magenta). Panels show representative high resolution scans of the cortical layers from the
1040 meninges and cortical layer 1 (at top), through layer II-VI to the corpus callosum (CC) at bottom. Note
1041 the reduced density of IBA1^{+} cells in the CC (demarcated by white dotted line) and apparent gradient
1042 through the cortical layers. **(B-F)** CD163 (green) was used to identify perivascular macrophages (PVM).
1043 Representative images of thalamus and cerebellum grey matter (GM) from wildtype and *Il34*$^{-/-}$ **(B&C)**
1044 and whole cortical scans **(E)** are shown. White dashed lines demarcate the meninges and arrows

1045 indicate direction towards CC. Data are presented as percentage area stained with CD163 in different
1046 brain regions with each dot representing an independent animal and scalebars representing 100 µm.
1047 Statistical analysis was performed using a One-way ANOVA followed by Tukey's test.

1048 **Figure 5. Selective loss of the microglial gene signature in multiple brain regions in *Il34*$^{-/-}$ rats.**

1049 mRNA was isolated from cortex, hippocampus (hipp) and thalamus (thal) of 12 week old *Il34*$^{+/+}$ and
1050 *Il34*$^{-/-}$ rats (N=4/genotype) and gene expression was quantified by RNA-seq as described in Materials
1051 and Methods. Network analysis to identify co-expressed gene clusters was performed using Graphia.
1052 The complete dataset and cluster analysis in provided in Table S1. Cluster 18 is the only cluster showing
1053 a relationship with *Il34* genotype. **(A)** The average tag per million (TPM) count of all genes from cluster
1054 18 identified by network analysis is represented as a bar for each sample sequenced. **(B)** Each panel
1055 shows expression of individual genes from cluster 18; each dot represents an independent sample
1056 (n=4). **(C)** Representative images of cortex from adult *Il34*$^{+/+}$, *Il34*$^{+/-}$ and *Il34*$^{-/-}$ brains (n=3/genotype)
1057 stained with IBA1 (red) and TMEM119 (green). **(D)** Expression of genes encoding microglial
1058 transcription factors (*Pu.1, Irf5, Irf8* and *Sall1*) and macrophage markers (*Cd74 and Cd68*).

1059 **Figure 6. Loss of IL34 does not affect pathology in the adenine-diet induced model of chronic kidney**
1060 **disease.**

1061 Cohorts of male and female rats were fed normal chow or a diet containing 0.2% adenine for 6 weeks.
1062 **(A)** Animal body weights were measured over the period of the adenine diet. **(B)** Water consumption
1063 by cage was quantified by comparing the difference in the weights of the bottle to the prior day, each
1064 line represents a single cage tracked longitudinally and "F" denotes female cages. **(C)** Water
1065 consumption at the cage level for the 5th week of the diet, each dot represents an independent cage
1066 black dots are male cages and brown dots are female cages(n≥4). **(D&E)** Serum Creatinine and urea
1067 were measured from serum collected through cardiac puncture. **(F)** The number of crystals in each
1068 kidney was quantified by calculating the area of the crystal across the entire kidney and normalized to
1069 the size of the kidney section quantified. **(G)** Sirius red staining was quantified as total stained area
1070 over the entire area of the kidney section quantified.

1071 **Figure 7. IL34-dependent macrophage expansion during chronic kidney injury**

1072 Cohorts of male and female rats were fed normal chow or a diet containing 0.2% adenine were stained
1073 for IBA1 and CD163. **(A-C)** Representative images for IBA1 in the medulla and cortex **(A&B)** and CD163
1074 in the medulla **(C)** are shown. **(D&E)** Medulla and cortex from IBA1 stained kidneys were quantified as
1075 percentage of area stained. **(F)** CD163 was only detected and quantified in the medulla. Slides were
1076 scanned on an Olympus slide scanner (VS120 or VS200) with a 40x objective and images captured with
1077 the Olyvia software. Scale bars represent 50μM.

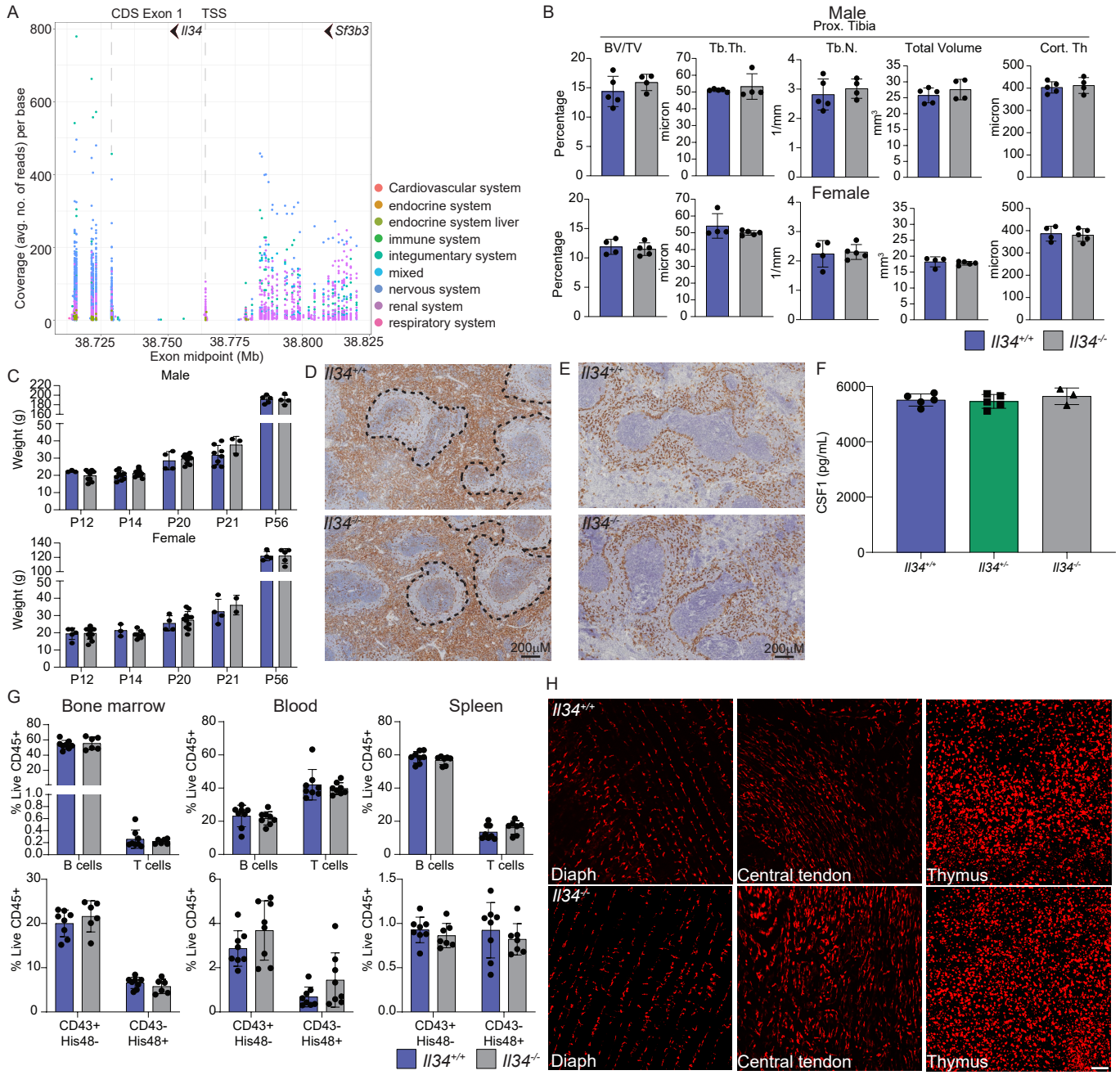
A
CDS Exon 1
TSS
Il34
Sf3b3
Coverage (avg. no. of reads) per base
Exon midpoint (Mb)
Cardiovascular system
endocrine system
endocrine system liver
immune system
integumentary system
mixed
nervous system
renal system
respiratory system
B
Male
Prox. Tibia
BV/TV
Tb.Th.
Tb.N.
Total Volume
Cort. Th
Percentage
micron
1/mm
mm³
Female
Il34+/+
Il34-/-
C
Male
Female
Weight (g)
P12
P14
P20
P21
P56
D
E
200µM
F
CSF1 (pg/mL)
Il34+/-
G
Bone marrow
Blood
Spleen
% Live CD45+
B cells
T cells
CD43+ His48-
CD43- His48+
H
Diaph
Central tendon
Thymus

Figure 1

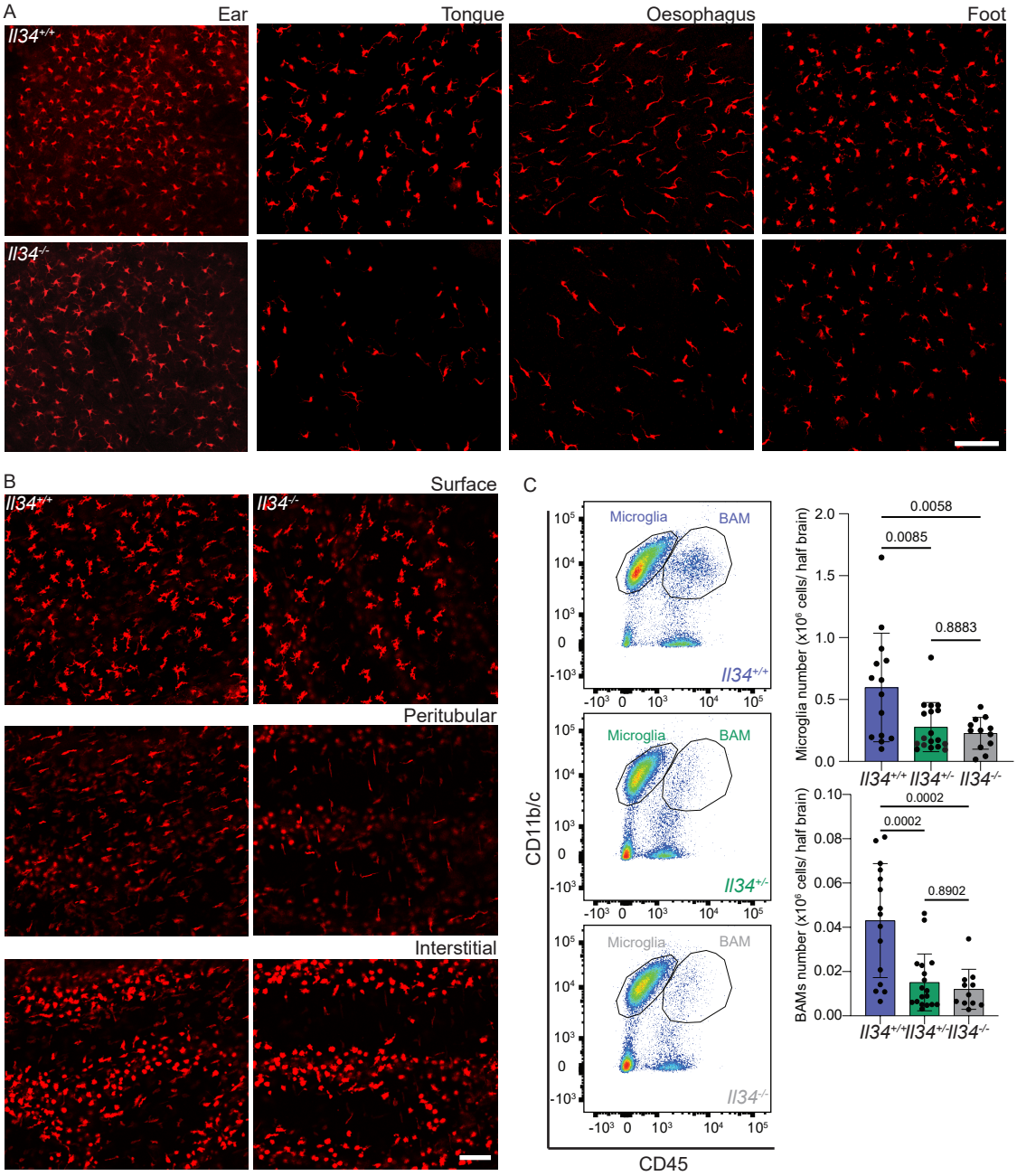
A
Ear
Tongue
Oesophagus
Foot
Il34+/+
Il34-/-
B
Surface
Peritubular
Interstitial
C
Microglia
BAM
Il34+/+
Il34+/-
Il34-/-
CD11b/c
CD45
Microglia number (x10^6 cells/ half brain)
BAMs number (x10^6 cells/ half brain)
0.0058
0.0085
0.8883
0.0002
0.0002
0.8902

Figure 2

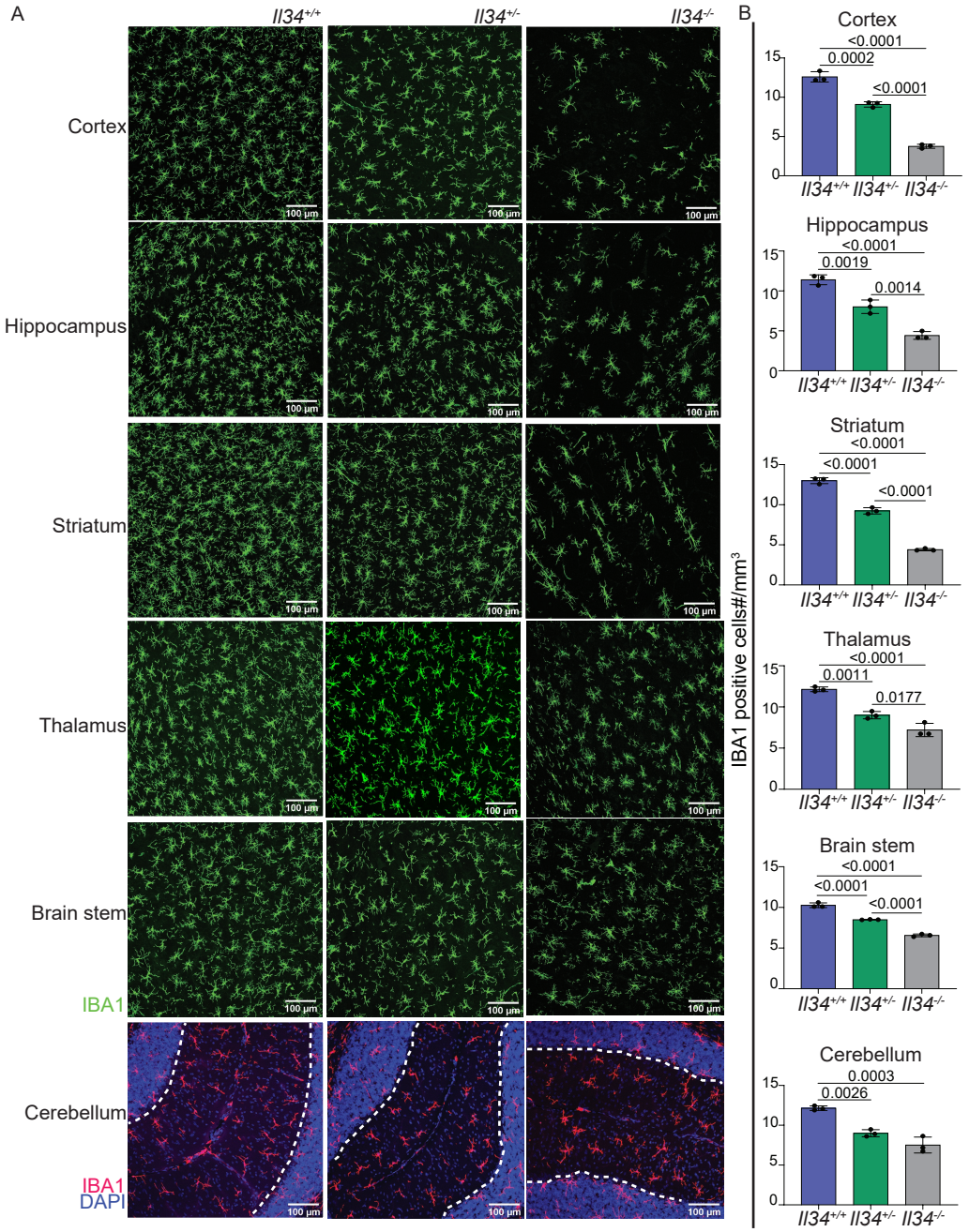
A
Il34+/+
Il34+/-
Il34-/-
Cortex
Hippocampus
Striatum
Thalamus
Brain stem
IBA1
Cerebellum
IBA1
DAPI
100 µm
B
IBA1 positive cells#/mm3
Cortex
<0.0001
0.0002
<0.0001
Hippocampus
<0.0001
0.0019
0.0014
Striatum
<0.0001
<0.0001
<0.0001
Thalamus
<0.0001
0.0011
0.0177
Brain stem
<0.0001
<0.0001
<0.0001
Cerebellum
0.0003
0.0026
0
5
10
15
Il34+/+ Il34+/- Il34-/-

Figure 3

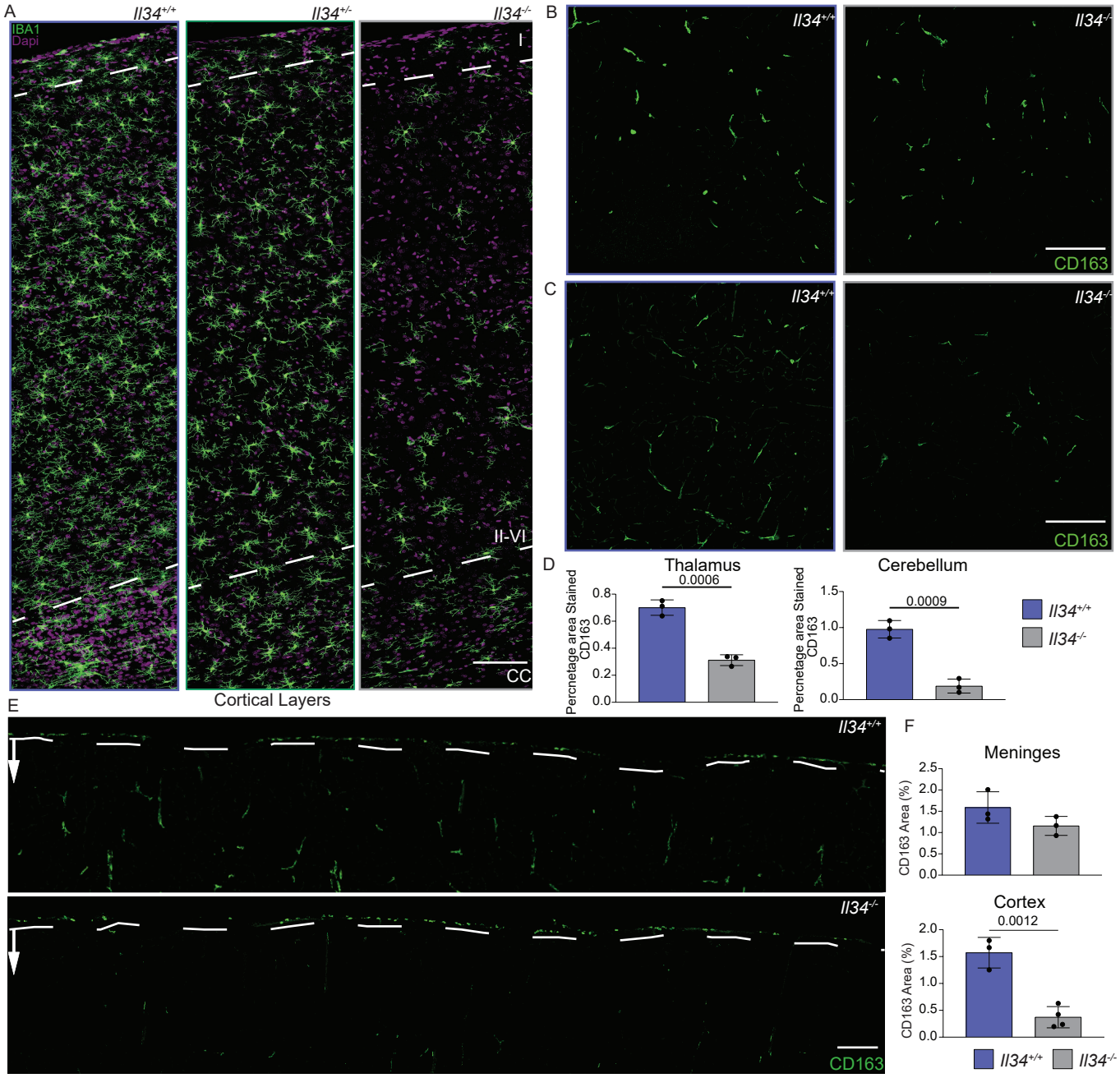
A
Il34+/+
Il34+/-
Il34-/-
IBA1
Dapi
I
II-VI
CC
Cortical Layers
B
Il34+/+
Il34-/-
CD163
C
Il34+/+
Il34-/-
CD163
D
Thalamus
0.0006
Percnetage area Stained CD163
0.8
0.6
0.4
0.2
0.0
Cerebellum
0.0009
Percnetage area Stained CD163
1.5
1.0
0.5
0.0
Il34+/+
Il34-/-
E
Il34+/+
Il34-/-
CD163
F
Meninges
CD163 Area (%)
2.5
2.0
1.5
1.0
0.5
0.0
Cortex
0.0012
CD163 Area (%)
2.0
1.5
1.0
0.5
0.0
Il34+/+
Il34-/-

Figure 4

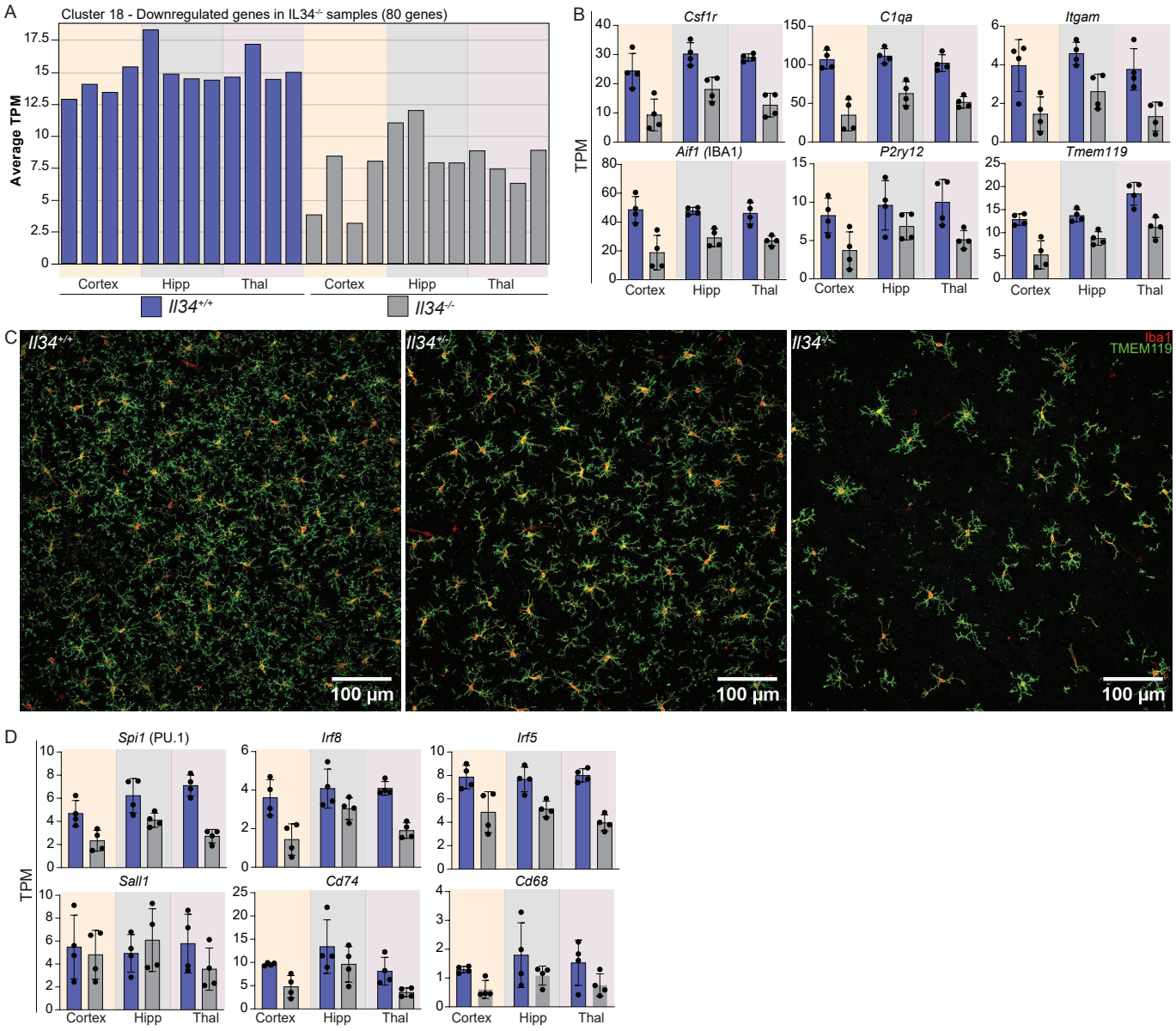
A
Cluster 18 - Downregulated genes in IL34-/- samples (80 genes)
Average TPM
Cortex
Hipp
Thal
Il34+/+
Il34-/-
B
Csf1r
C1qa
Itgam
Aif1 (IBA1)
P2ry12
Tmem119
TPM
C
Il34+/+
Il34+/-
Il34-/-
Iba1
TMEM119
100 µm
D
Spi1 (PU.1)
Irf8
Irf5
Sall1
Cd74
Cd68

Figure 5

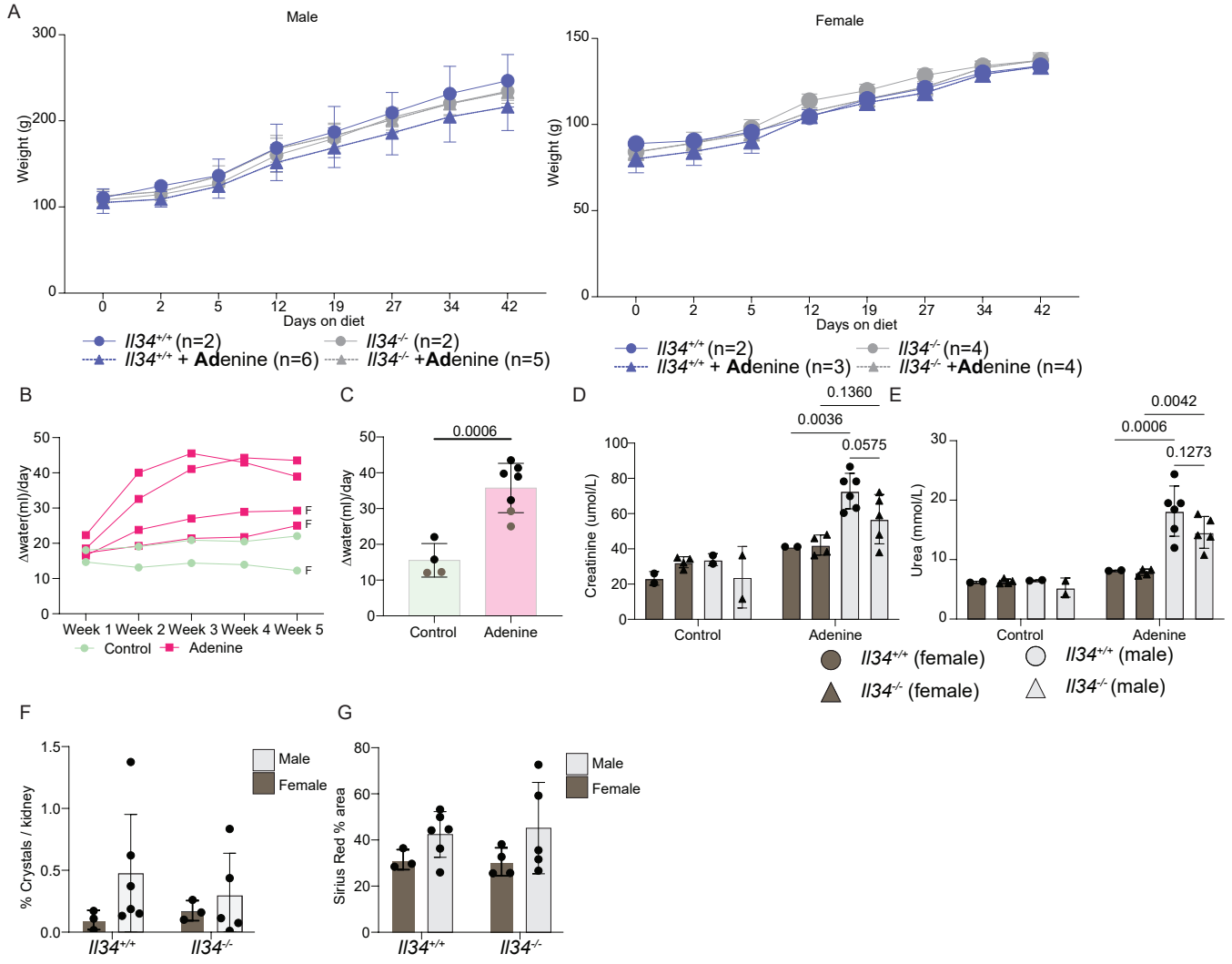
A
Male
Weight (g)
Days on diet
Il34+/+ (n=2)
Il34+/+ + Adenine (n=6)
Il34-/- (n=2)
Il34-/- +Adenine (n=5)
Female
Il34+/+ (n=2)
Il34+/+ + Adenine (n=3)
Il34-/- (n=4)
Il34-/- +Adenine (n=4)
B
Δwater(ml)/day
Week 1 Week 2 Week 3 Week 4 Week 5
Control
Adenine
C
0.0006
Control
Adenine
D
0.1360
0.0036
0.0575
Creatinine (umol/L)
E
0.0042
0.0006
0.1273
Urea (mmol/L)
Il34+/+ (female)
Il34-/- (female)
Il34+/+ (male)
Il34-/- (male)
F
% Crystals / kidney
Male
Female
G
Sirius Red % area

Figure 6

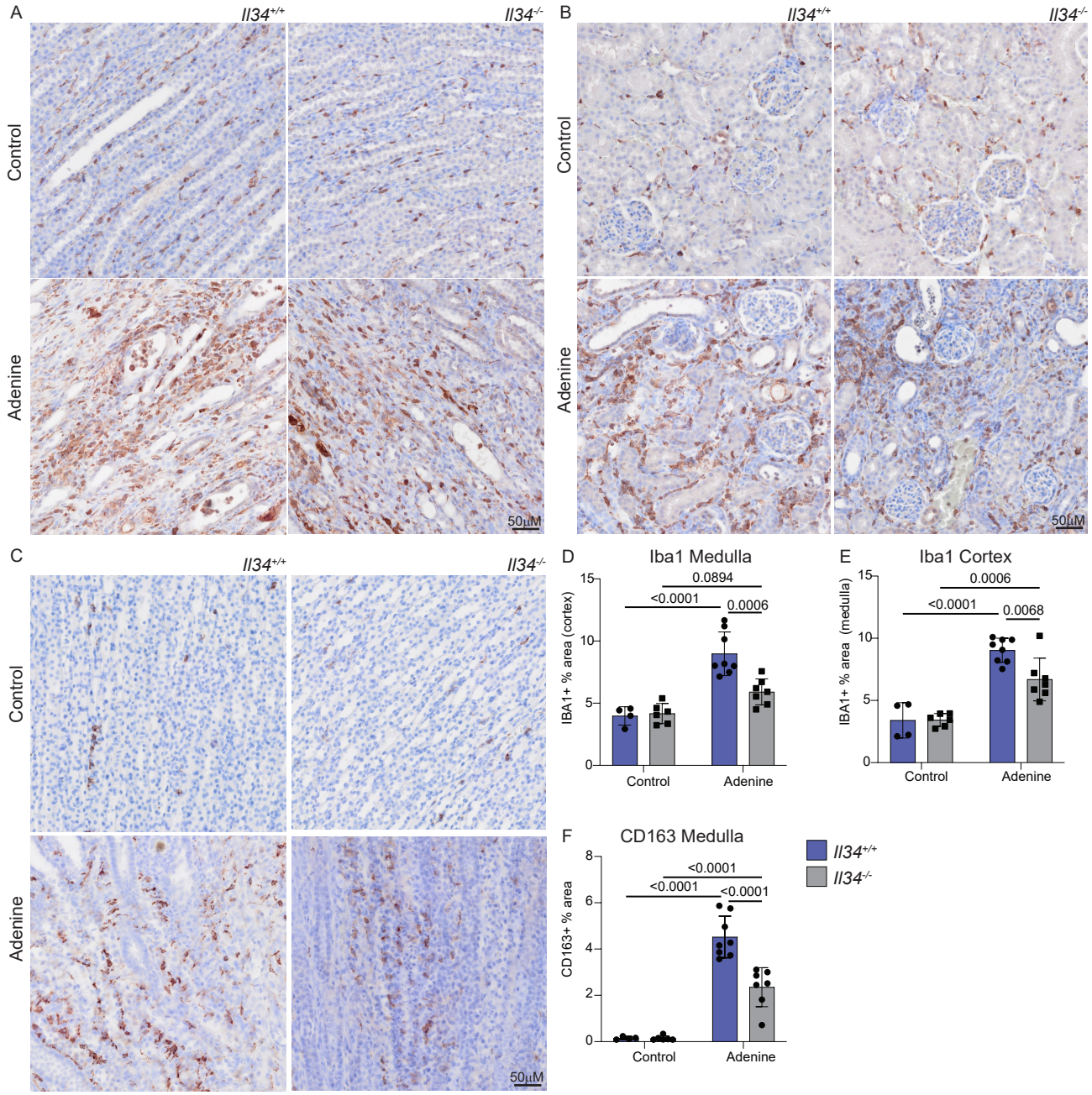
A
Il34+/+
Il34-/-
Control
Adenine
50µM
B
Il34+/+
Il34-/-
Control
Adenine
50µM
C
Il34+/+
Il34-/-
Control
Adenine
50µM
D
Iba1 Medulla
IBA1+ % area (cortex)
0.0894
<0.0001
0.0006
Control
Adenine
E
Iba1 Cortex
IBA1+ % area (medulla)
0.0006
<0.0001
0.0068
Control
Adenine
F
CD163 Medulla
CD163+ % area
<0.0001
<0.0001
<0.0001
Control
Adenine
Il34+/+
Il34-/-

Figure 7